

From time dependent incorporation of molecular building blocks to application properties for inorganic and organic three-dimensional network polymers

Lies De Keer

Ghent University

Karsu Kilic

Stanford University

Paul Van Steenberge

Ghent University

Lode Daelemans

Ghent University <https://orcid.org/0000-0001-6214-3785>

Daniel Kodura

Queensland University of Technology

Hendrik Frisch

Queensland University of Technology

Karen De Clerck

Ghent University

Marie-Françoise Reyniers

Ghent University

Christopher Barner-Kowollik

Queensland University of Technology <https://orcid.org/0000-0002-6745-0570>

Reinhold Dauskardt

Stanford University

Dagmar D'hooge (✉ Dagmar.Dhooge@UGent.be)

Ghent University <https://orcid.org/0000-0001-9663-9893>

Article

Keywords: three-dimensional network polymers, Monte Carlo simulations, Diels-Alder based networks

Posted Date: November 12th, 2020

DOI: <https://doi.org/10.21203/rs.3.rs-98270/v1>

License:  This work is licensed under a Creative Commons Attribution 4.0 International License.

[Read Full License](#)

From time dependent incorporation of molecular building blocks to application properties for inorganic and organic three-dimensional network polymers

L. De Keer,¹ K. I. Kilic,² P.H.M. Van Steenberge,¹ L. Daelemans,³ D. Kodura,⁴ H. Frisch,⁴ K. De Clerck,³ M.F. Reyniers,¹ C. Barner-Kowollik,^{4,5} R. H. Dauskardt,^{2*} D.R. D'hooge^{1,3*}

¹Laboratory for Chemical Technology (LCT), Ghent University, Technologiepark 125, 9052 Ghent, Belgium

²Department of Materials Science and Engineering, Stanford University, 416 Escondido Mall, Stanford, CA 94305-2205, USA

³Centre for Textiles Science and Engineering (CTSE), Ghent University, Technologiepark 70a, 9052 Ghent, Belgium

⁴Centre for Materials Science, School of Chemistry and Physics, Queensland University of Technology (QUT), 2 George Street, Brisbane QLD, 4000, Australia

⁵Macromolecular Architectures, Institut für Technische Chemie and Polymerchemie (ITCP), Karlsruhe Institute of Technology (KIT), Engesserstrasse 18, 76128, Karlsruhe, Germany

Abstract

The three-dimensional configurational arrangement of natural and synthetic network materials determines their application range. Control of the real time incorporation of each building block, hence, all functional groups is desired so that we can regulate macroscopic properties from the molecular level onwards. Here we interconnect kinetic Monte Carlo simulations from the field of chemical kinetics and molecular dynamic simulations from the field of physics. We visualize for (in)organic network material synthesis how the initial building blocks interact timewise and spatially, accounting for variations in inter- and intramolecular chemical reactivity, diffusivity, segmental compositions, branch/network point locations, and defects. We use the kinetic and three-dimensional structural information to construct structure-property relationships based on molecular descriptors such as the molecular pore size or dangling chain distribution, differentiating between ideal and non-ideal structural elements. The generic nature is illustrated by constructing such relationships for the synthesis of organosilica, epoxy-amine and Diels-Alder based networks.

Essential for network materials is the degree of three-dimensional (3D) configurational ordering or arrangement, as it determines their macroscopic property and application range.¹⁻⁴ Highly ordered carbon atom (C) arrangements possess e.g. an exceptional behavior with diamond (sp^3 hybridization; Fig. 1a) and graphite (sp^2 hybridization) respectively known for their hardness and lubricating potential.⁵⁻⁶ Another example is a synthetic zeolite with its ordered molecular pore structure allowing shape selectivity of catalyzed chemical reactions.^{7,8}

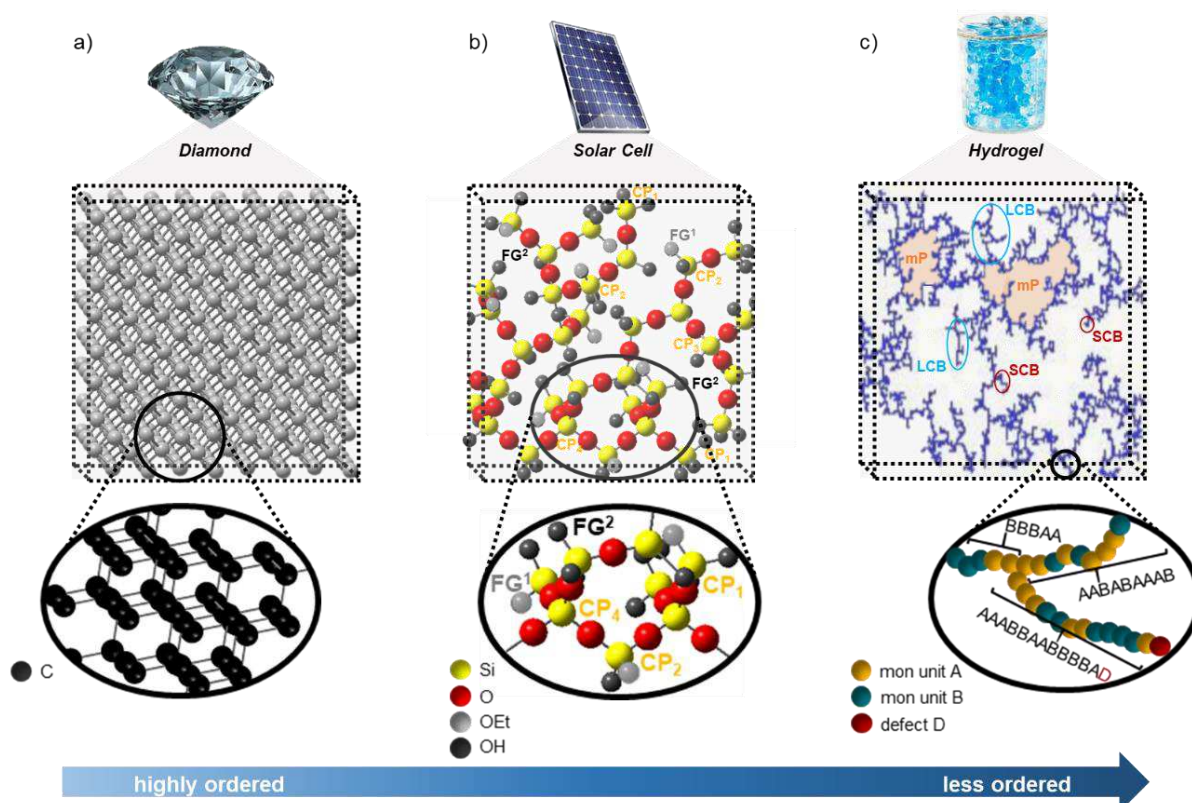


Fig. 1: Network materials with decreasing order of their 3D structural configuration. **a** perfectly ordered carbon (C) atoms in sp^3 hybridization, as in diamonds. **b** highly ordered silica atoms with oxygen (O) bridges in sp^3 hybridization with a limited number of structural defects, as in solar cells. Examples of such defects are unreacted functional groups (FG¹ = OEt, FG² = OH; Et= ethyl), leading to incomplete crosslinking points (CP's; CP₁ = CP with *i* crosslinks). **c** highly random configurations of (co)monomer units (mixture of sp^3 and sp^2 hybridization) containing atoms such as C, O and nitrogen (N), and functional groups leading to network molecules with different segment lengths and many structural defects (e.g. dangling chains: short and long branches (S/LCB's), and inverse monomer insertions), as in hydrogels; examples of molecular pores (mP's) are colored in light orange; the building blocks are symbolized by colored spheres that represent atoms (in a and b) and a chemical moiety such as a targeted comonomer unit A/B or side reaction defect D (in c).

Less ordered configurations also exist with a prominent role for natural polymers such as cellulose and lignin forming plant cell walls,⁹ and network polymers synthesized from oil-derived or renewable (co)monomers.¹⁰⁻¹⁶ For example, organosilica networks as employed for solar cells, separation

technologies, and antimicrobial coatings¹⁰⁻¹² are formed by polycondensation but with unavoidable structural defects such as incomplete silica-oxygen-silica (Si-O-Si) crosslinks, as shown in Fig. 1b with the CP_i label denoting a crosslinking point (CP) with i crosslinks. More structural defects and 3D randomness are encountered in organic chain-growth based hydrogels for hygiene products, tissue engineering scaffolds, and drug delivery devices.¹³ This randomness is caused by the higher number of side reactions with different reactivities and the more complex reactant structure involving more atoms than simply C (or Si) and a plethora of functional groups.¹⁴⁻¹⁶ As shown in Fig. 1c, in hydrogels, a mixture of sp^3 and sp^2 hybridizations is obtained accompanied by many structural defects, likely several branch types and inverse monomer insertions. Network segments with a broad spectrum of monomer sequences (e.g. AAABBAABBBBA, BBBAA, AABABAAAB, ... with A and B the comonomer units) can be also identified that are either defining a 3D molecular pore (light orange color) or a dangling branch located at a certain 3D position. These dangling chains can crosslink or form network segments by inter- or intramolecular reactions but can also be too restricted in diffusivity to take part in such network formation. Moreover, the regular A/B connectivity can be disturbed due to the formation of units with structural defects (e.g. the label D in the zoom of Fig. 1c).

In the present work, we fully acknowledge this broad spectrum of both ideal and non-ideal structural elements^{14,17,18} to predict and regulate network polymer macroscopic properties at the molecular level, already during the synthesis. Starting from the original functional molecules or building blocks we target the spatial thus 3D incorporation of all individual functional groups, segments, and structural defects at any synthesis time, hence, from the first second to the end of the synthesis, e.g. several hours later on. This goes beyond the state-of-the art in which experimental and theoretical methodologies never jointly cover all relevant synthesis time dependent phenomena such as (i) the kinetic and thermodynamic interplay of chemical reactivities and molecular diffusion, due to the increasing viscosity and gel formation along the complete synthesis, and (ii) the continuous 3D variation of compositional and topological combinations, including structural defects, upon the incorporation of each building block.

Conceptual framework from molecular to material and ultimately application level

Experimental methodologies are typically delivering information at scales larger than the molecular one with chromatography and mass spectrometry not automatically applicable and analytical methods such as solid-state nuclear magnetic resonance spectrometry providing only bulk information.^{17,19,20} Sometimes average characteristics such as the overall comonomer content and the number of branching points per (co)monomer unit can be measured for specially modified reactants¹⁹ but in general practical limitations exist to access structural deviations between and within network molecules.

Theoretical methodologies also face restrictions with, in the research field of chemical kinetics, emphasis on overall thus averaged synthesis time dependencies for the (co)monomer/functionality incorporation. The temporal evolutions of the reactant, intermediate and product concentrations have been addressed considering side reactions but are often limited to the time region before the gel point. Only rarely 2D connectivities of the CP's or clustering in (graph) node notation have been aimed at^{21,22} but in any case a 3D network configuration has not been calculated. Most promising is our recently developed matrix-based kinetic Monte Carlo (*k*MC) methodology, which upon experimental validation considering average characteristics (*e.g.* the number average chain length and dispersity)^{16,23} and inputted individual kinetic parameters from independent experimental techniques,²⁴ allows to access (co)monomer sequences of a representative number of individual (*e.g.* 10^4 - 10^5) linear or slightly branched chains.^{14,25,26}

Also in the physics research field, simplifications have been made with force-field-based molecular dynamic (MD) simulations mostly predicting ideal defect-free 3D network structures at high monomer conversion often neglecting molecular kinetic constraints. A key MD assumption is the free movement of atoms or atom groups until the thermodynamically equilibrated configuration is reached, typically recognizing a limited number of chemical bond types and thus ignoring many side (*e.g.* intramolecular) reactions and diffusivity constraints.^{10,27-32} For the equilibrium settling, MD simulations implicitly assume a generally incorrect large real time. Free radical based organic networks are *e.g.* produced on a minute to hour scale with altering dynamic viscosity (η), leading to time and chain length dependent

diffusivities. This prevents the final configuration from reaching thermodynamic equilibrium for the complete 3D network, causing structural defect formation which influences the material properties.^{3,33}

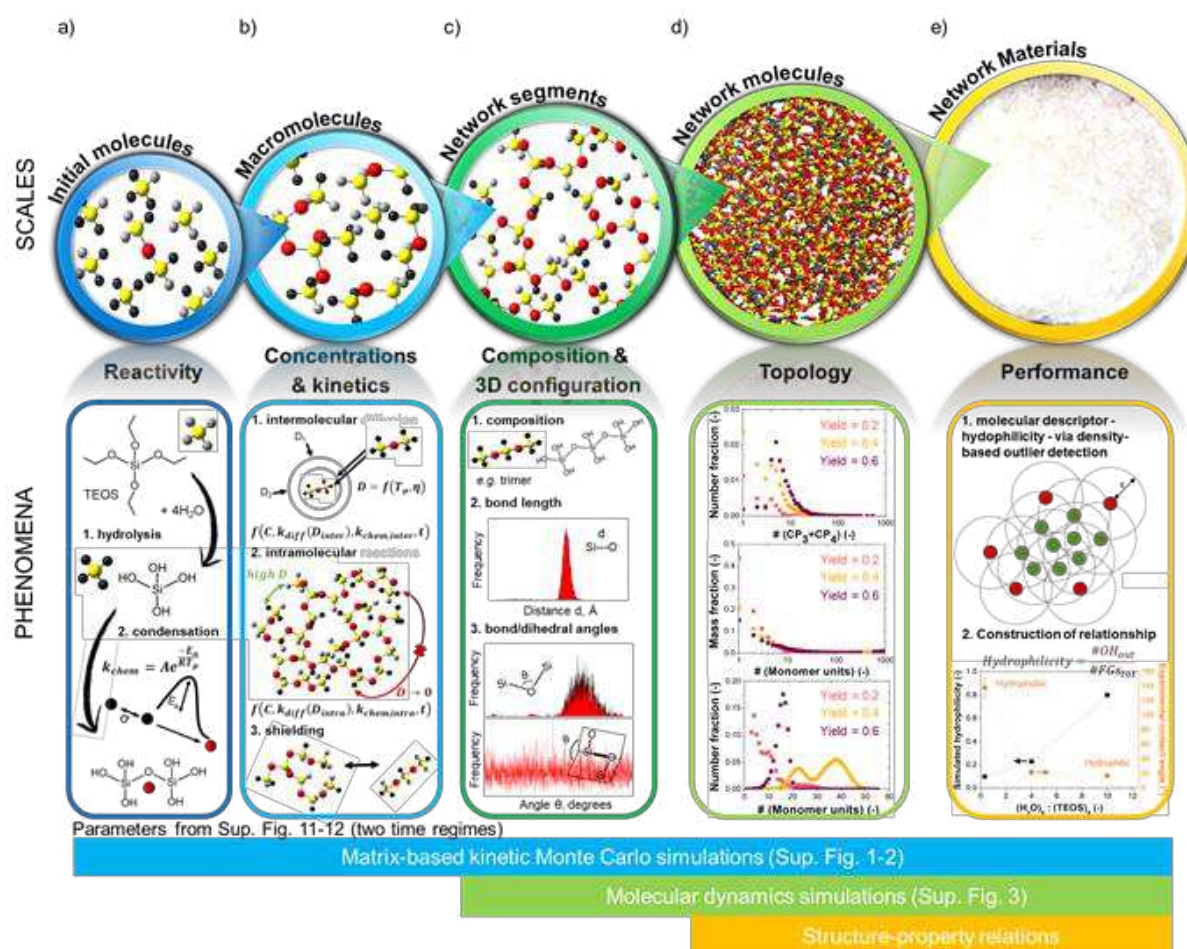


Fig. 2: Main concepts of framework to design network polymer synthesis starting at the molecular scale; matrix-based kinetic Monte Carlo (*kMC*) and molecular dynamic (MD) simulations are interconnected to visualize the incorporation of building block by building block so each functional group (FG) at any synthesis time t ; illustration for organosilica network synthesis (Fig. 1b) commencing from tetraethylorthosilicate (TEOS). **a** molecular scale with chemical rate coefficients for main and side reactions (k_{chem} values; Arrhenius parameters A and E_a ; reaction distance σ ; polymerization temperature T_p and pressure p_p). **b** chemical kinetics with calculation of inter/intramolecular rates ($r_{\text{inter/intra}}$; (mol L^{-1}) s^{-1}) from concentrations of reactants, intermediates and products (C values) accounting for interplay of inter/intramolecular reactions and diffusivities (D : diffusion coefficient; η : dynamic viscosity; k_{diff} : diffusion rate coefficient). **c** *kMC* data storage and update of compositions, including segments, structural defects, and connectivities of crosslinking points (CP's). Combined with MD data on bond/dihedral angles and bond lengths 3D configurations for each molecule result at any t accounting for non-idealities thus defects. **d** in silico derived molecular network characteristics up to topological scale at any t ; examples are CP distribution (at least 3 crosslinks; CP_3+CP_4), molar mass distribution, and molecular pore size distribution. **e** characteristics from d serve as input to construct structure-property relationships that evaluate the network material performance, with a possible differentiation between ideal and non-ideal structural network elements. Example of hydrophilicity calculation based on the presence of OH functional groups near the surface (see Supplementary Methods).

In the present work, we connect the fields of chemical kinetics and physics by developing a generic framework according to the principles in the Methods section to visualize the spatial kinetic growth of network polymers at the molecular level so that we can fully grasp the birth of their 3D nature and the further inter/intramolecular interactions and chemical modifications. Matrix-based *k*MC and MD simulations are uniquely combined to store at any synthesis time *t* the molecular information on individual (segment) compositions, functional groups, bond lengths, bond and dihedral angles, and structural defects. As shown in Fig. 2, the step by step incorporation of each building block thus functional group is accounted for while grasping at various length scales (top row) the essential fundamental phenomena (bottom row) through step-wise experimental validation. Focus is on the synthesis of organosilica networks (Fig. 1b), commencing with a sufficiently large number of tetraethylorthosilicate (TEOS) molecules as *k*MC ensemble (e.g. $10^5 - 10^6$).

As shown in Fig. 2a, the initial TEOS molecules can be hydrolyzed multiple times (top of box) and take part in subsequent condensation reactions, resulting in the formation of Si-O-Si crosslinks (bottom of box). In general, a differentiation is made between inter- and intramolecular crosslinking reactions altering the local network make-up. The intermolecular reactions bridge network molecules so that a large(r) network molecule is formed but also deplete the linear molecules by their inclusion as dangling chains in an already existing network molecule or by the creation of branched still non-crosslinked species. The intramolecular reactions increase the crosslinking degree within a given network molecule through cyclization. They are more likely at higher polymer network yields³⁴ and lead to structural defects often denoted as internal loops.³⁵ Every reaction step in Fig. 2a, as defined by the involved functional groups, is characterized by Arrhenius parameters (*A* and *E_a* values) so that at a given polymerization temperature (*T_p*) and pressure (*p_p*) chemical rate coefficients (*k_{chem}* values) describing intrinsic chemical reactivities can be obtained. Regression to experimental data using monofunctional analogues or limited to low crosslinking yields is most suited to determine *k_{chem}* values, linking via kinetic modeling analysis the dominance of specific reactions to specific time regimes for certain experimental responses. The number of unreacted groups of a network moiety (or building block) can influence *k_{chem}* values of the remaining functional groups, as shown in Supplementary Figure 11.

Besides the k_{chem} values in Fig. 2a the concentration (C) variations of all molecule types are required thus from monomer to dimer and ultimately network molecules, addressing the spectrum in functional group types and combinations. As shown in Fig. 2b, inter- and intermolecular reaction rates ($r_{\text{inter/intra}}$) are calculated that are corrected for diffusional limitations. For larger η values, the intermolecular reactivities can be even fully dictated by chain length and CP dependent diffusivities (D_{inter} values).¹⁴ Intermolecular apparent rate coefficients (k_{app} instead of k_{chem} values) are therefore introduced to grasp the interaction of intrinsic kinetics and diffusional constraints.³⁶ Intramolecular Si-O-Si crosslinking in turn becomes impossible if the distance between the functional groups is too large (red vs. green arrows in Fig. 3b), since the intramolecular diffusion coefficients on the functional group level (D_{intra} values) are then too low. Fundamental distance rules accounting for rigidity, as codictated by the number of CP's between functional groups, are therefore introduced.

During the calculation of $r_{\text{inter/intra}}$ values, which are function of k_{chem} and C variations, we keep track of the connectivity history of all molecules in the $k\text{MC}$ ensemble through a composite topology matrix T . In this way, we can retrieve at any t extensive molecular distributed data regarding (i) the composition of remaining and formed linear/branched molecules, and (ii) the segment compositions, including structural defects, and the connectivities of each separate network molecule (Fig. 2c; top). Combined with MD simulation input a 3D representation of these individual (network) molecules is within reach. MD simulations allow to access the spectrum of bond and dihedral angles, and bond lengths that are thermodynamically feasible,¹⁰ as illustrated in Fig. 2c (bottom). Hence, by following each connectivity in the $k\text{MC}$ matrix T the local environment can be scanned and a feasible thus stable 3D structural element can be generated if no structural defect is detected. Upon doing so alternative 3D visualization rules are needed to ensure the correct representation of the non-ideality in the 3D network structure. The unique combination of $k\text{MC}$ and MD data (Fig. 2a-c) therefore enables to visualize the 3D configuration of network molecules as a function of t covering both ideal and non-ideal building block incorporations. Notably MD simulations deliver input data for the $k\text{MC}$ algorithm and, hence, any further development in the physics field, e.g. the improved description of polymer-medium interactions, can be directly translated in the current multi-scale development.

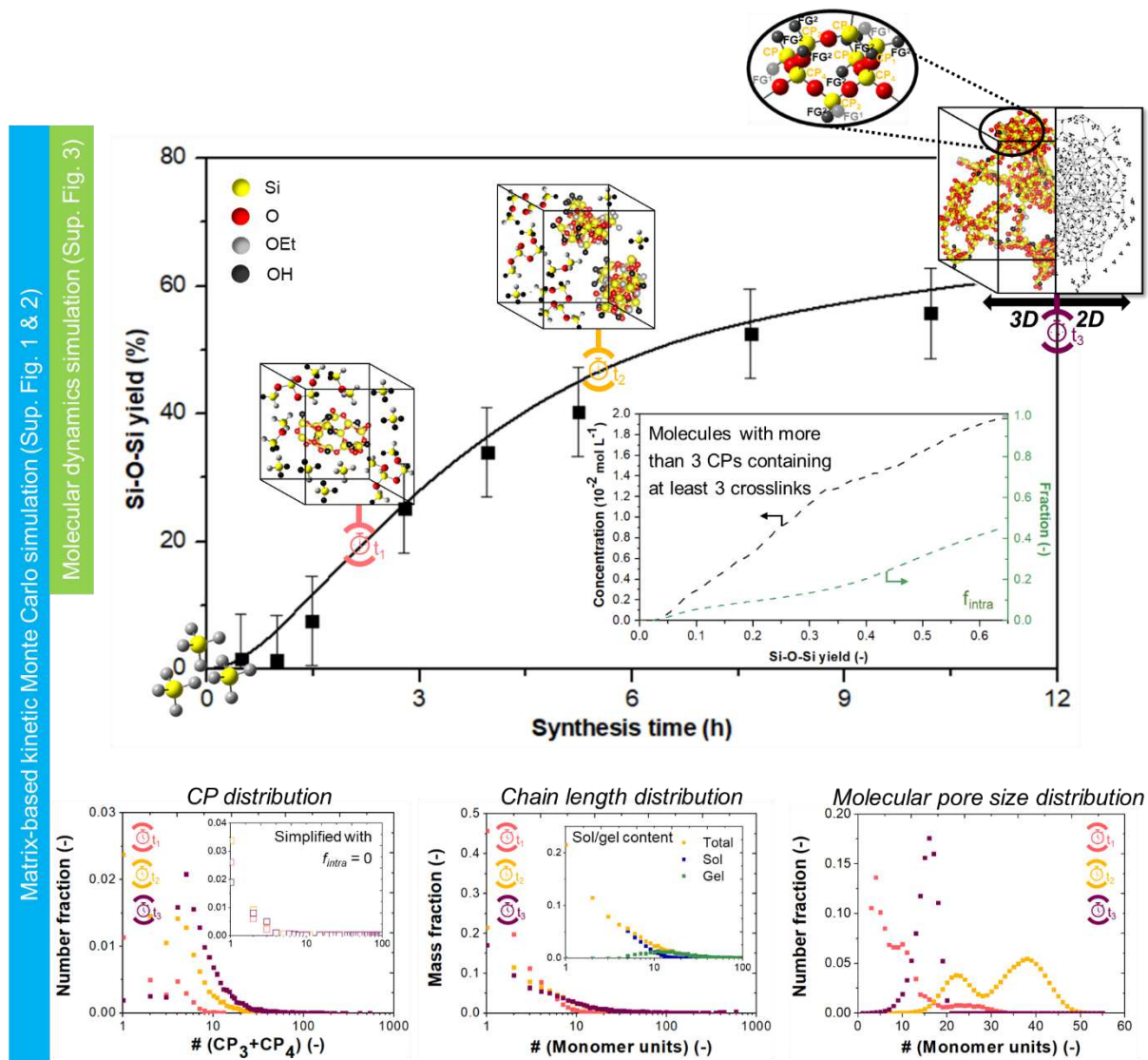


Fig. 3: Strength of connecting matrix-based kinetic Monte Carlo (kMC) and molecular dynamic (MD) simulations to fundamentally understand time dependencies for organosilica network synthesis, starting from tetraethylorthosilicate (TEOS); (top part) with (i) main graph focusing on birth and 3D growth of network molecules as a function of synthesis time t (298 K); yield: Supplementary Equation 5; initial conditions and model parameters: Supplementary Table 1; model validation: Supplementary Figure 11 and 12; experimental yield data;³⁷ with increasing t more building blocks incorporated but also defects manifested, as tracked according the concepts in Fig. 2 (flow sheets: Supplementary Figure 1-3); and with (ii) lower graph depicting the concentration variation of molecules with > 3 crosslinking points (CP's; CP_3+CP_4) alongside f_{intra} the (cumulative) fraction of intramolecular contributions; FG: functional group; (bottom part) 3 boxes focusing on three synthesis times (t_1 , t_2 and t_3) giving examples of associated distributed molecular descriptors: left to right: (i) number CP distribution summing up the contributions of CP_3 and CP_4 (inset simplified $f_{intra}=0$); (ii) mass chain length distribution (CLD: monomer unit: building block), including in inset for t_2 the distinction between sol (linear/loosely branched chains) and gel (precipitated molecules) with for molecules as cut-off to belong to gel the ratio of number of CP's to number of monomer units larger than 0.5; (iii) number molecular pore size distribution with the pore size related to number of monomer units in the pore; 10% error bar.

As highlighted in Fig. 2d-e, the detailed 3D molecular information from Fig. 2a-c can be utilized to construct fundamental structure-property relationships in which the dependent variables are detailed

molecular network descriptors coming from explicit distributions. Examples of such distributions are the CP connectivity, dangling chain, functional group distance, and molecular pore size distribution, with a possible differentiation between the contribution of ideal and non-ideal structural network elements. Upon recording experimental macroscopic responses for instance at various t values we can thus identify the main network molecular descriptors for material design and future development so that the synthesis conditions can be tuned toward a controlled balance of main and side reactions, and of chemistry and viscosity variations. This t dependency constitutes the strength of the framework, as macroscopic property design is achieved whenever desired not restricted to current simplified cases of limiting crosslinking or ideally constructed high yield (theoretical) polymer networks.

Application of framework for time dependencies in organosilica network synthesis

Fig. 3 displays the strength of the in Fig. 2a-c outlined framework to fundamentally characterize and understand organosilica synthesis, starting from TEOS building blocks (chemistry 1 in the Methods section). The initial conditions and model parameters are highlighted in Supplementary Table 1, with the parameters determined based on literature experimental data.³⁷ This is explained in the Supplementary discussion, performing model validation using specific experimental responses for two time regimes, one related to hydrolysis and one to polycondensation (Supplementary Figure 11 and 12).

The top part of Fig. 3 depicts the traditional Si-O-Si experimental and simulated yield (Supplementary Equation 5; points vs. full line) as a function of t . At t_1 , t_2 , and t_3 the 3D visualization of a representative number of network molecules is included, with at t_3 the simplified 2D visualization as well. For kinetic interpretation, a lower graph addresses the t variation of (i) the concentration of specifically network molecules with more than 3 CP's possessing in turn 3 or 4 crosslinks (CP₃+CP₄; left axis; black); and (ii) the fraction of intramolecular reactions (f_{intra} ; right axis; green). Derived distributed molecular descriptors are provided for these times at the bottom part of Figure 3, considering (i) the number (CP₃+CP₄) distribution, (ii) the mass chain length distribution, and (iii) the number molecular pore size distribution. An inset is added for the (CP₃+CP₄) distribution displaying theoretical results for $f_{\text{intra}} = 0$ and for the chain length distribution, at t_2 , a split-up is made regarding the contribution of the sol (blue symbols) and the gel (green symbols). Molecules with their number ratio of (CP₃+CP₄) over the number

of monomer units larger than 0.5 are forming the gel, as clear from the sensitivity analysis in Supplementary Figure 21. Each pore size is expressed by the number of monomer units defining a closed loop, as explained in the Supplementary discussion.

We can see in Fig. 3 that at low yield a gradual transition from a linear to a slightly crosslinked polymer is obtained that is fully converted in a network material at high yield, as evidenced by the increasing fraction of network molecules with more than 3 CP's containing at least 3 crosslinks. A high degree of structural heterogeneity is always established. At small times (t_1) the CP connectivity distribution is less-defined particularly for molecules with less crosslinking, whereas at larger times (t_2 and t_3) the non-ideality is also established at the tail as evident upon comparison with the inset results ($f_{\text{intra}}=0$) displaying different contributions of more crosslinked molecules. Such tail variation is also valid for the chain length distribution, indicative of a continuous compositional variation. The molecular pore size distribution first develops a bimodal character (t_1 to t_2), as f_{intra} increases from 0 to a significant value so that more pores are formed from smaller molecules, to then at larger time (t_3) lose this bimodality accompanied by a shift to the left as many smaller pores are created by a dominance of intramolecular reactions. Similar non-trivial molecular property dynamics are depicted in Supplementary Figure 20, addressing the CP distance distribution, and the average crosslinking density and number/mass chain length variation. Hence, t dependencies strongly alter the molecular build-up so that synthesis conditions are essential in network material design.

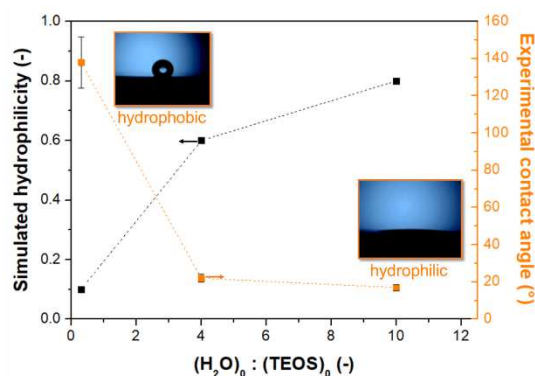
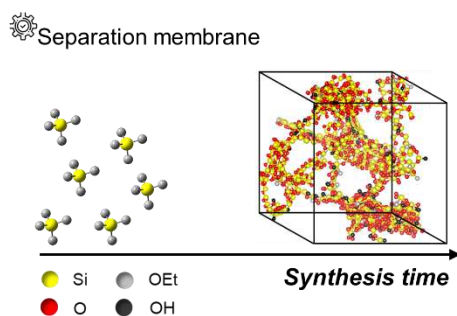
Discussion

As shown in Fig. 4, even upon focusing only on conventional macroscopic properties such as the contact angle, the storage modulus, and the swelling degree bearing in mind applications such as membrane separation,¹² coatings,³⁸ and drug delivery,¹³ the developed framework provides added value in molecular scale interpretation and design. In Fig. 4a, emphasis is still on the organosilica case dealing with 3 high yield (70%) 3D ensembles as *in silico* generated for 3 initial sets of conditions that differ in the initial H₂O amount but with otherwise conditions as in Fig. 3. For one such ensemble (initial water to TEOS molar ratio of 4) the 3D structure is depicted in the left part of Fig. 4a. Post-processing using density-based outlier detection,³⁹ as explained in the Supplementary Discussion, allows calculating the

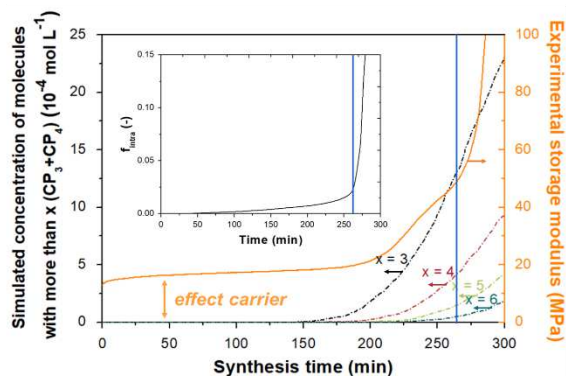
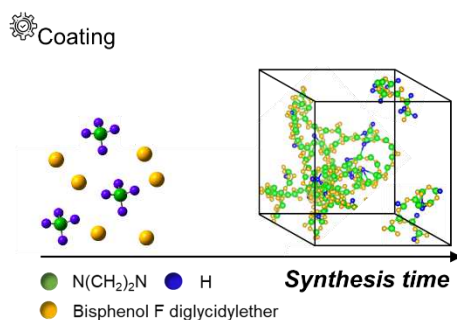
number of OH groups near the surface so that the hydrophilicity can be simulated as normalized with respect to the total number of functional groups. These simulated hydrophilicities are displayed in the right part of Fig. 4a (left axis; black symbols) and correlate with measured contact angles (right axis; orange symbols).⁴⁰ A larger simulated hydrophilicity implies a better interaction with the surface thus better wetting so that the experimental contact angle decreases. A closer inspection of Fig. 4a, however, reveals that the conventional contact angle is only sensitive in the region of lower to intermediate hydrophilicities (up to 60%), which is associated with initial water to TEOS molar ratios smaller than or equal to 4. The simulation results although show that higher initial molar ratios are experimentally useful if one wants to maximize the availability of OH groups near the surface (> 60%), as for instance crucial for molecular scale driven separation.^{12,41}

In Fig. 4b (right part), emphasis is on the molecular scale interpretation of the temporal evolution of the experimentally recorded storage modulus (right axis; orange) for epoxy-amine curing (network chemistry 2 in the Methods section) according to the initial conditions and model parameters listed in Supplementary Table 2 and the model validation in Supplementary Figure 13a. The developed framework allows to depict the associated variation of the concentration of molecules with more than x (3,4, 5 or 6) CP's containing at least 3 crosslinks (CP_3+CP_4 ; left axis; black) and f_{intra} . At small times the experimental material stiffness in Fig. 4b (right part) is very limited with steadily increasing but always low moduli. No significant network formation has taken place yet, as confirmed by the low simulated concentrations even for network molecules with a low number of crosslinks. As soon as a substantial number of molecules is formed with 3 CP's of the type CP_3 or CP_4 (black dashed-dotted line in Fig. 4b; left axis), the storage modulus increases significantly. Extra material rigidity/stiffness is gradually acquired at larger synthesis times, at which the contribution of molecules with more than 3 CP's of the type CP_3 or CP_4 becomes gradually more relevant (other lines in Fig. 4b; left axis). The steep increase at very large times although requires an extra molecular descriptor change, *i.e.* the elevated f_{intra} as marked by the blue vertical line in the upper graph. This additional increase does not follow from the conventional average crosslinking density increase, as shown in Supplementary Figure 22b, and again confirms the strength of the developed platform.

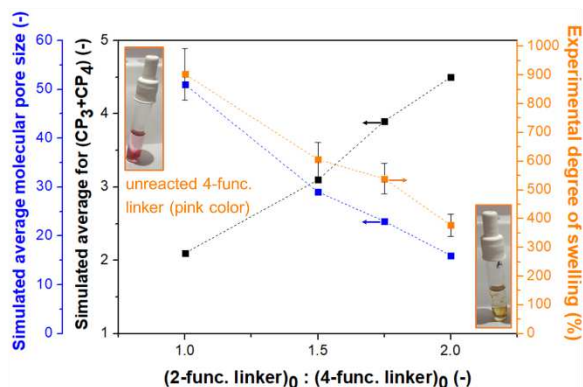
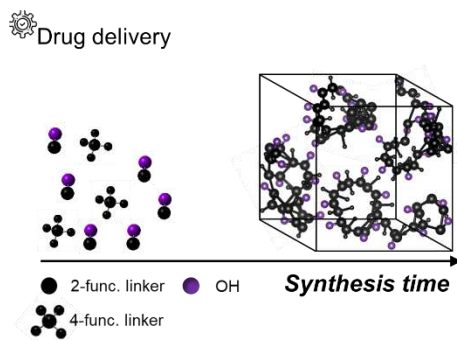
a) *Organosilica synthesis*



b) *Epoxy/amine curing*



c) *Diels-Alder chemistry*



Structure-property relations

Fig. 4: Structure-property relationships at molecular level. **a** application for organosilica case (network chemistry 1; initial and model parameters: Supplementary Table 1). Relation of initial molar ratio of water (H_2O) to tetraethylorthosilicate (TEOS) for synthesis (298 K) and simulated hydrophilicity at 70% yield (density-based outlier detection:³⁹ Supplementary Methods section for relative contribution of OH near surface) to understand the change in experimental contact angles⁴⁰ (orange; right axis) **b** application for epoxy-amine curing case (network chemistry 2; initial and model parameters: Supplementary Table 2). Explanation of temporal variation of experimentally recorded variation of storage modulus (orange; right axis; this work; initial storage modulus due to the flexible cuvette) based on simulated concentration of network molecules with more than x (3-6) crosslinking points (CP's) containing at least three crosslinks (left axis; $\text{CP}_3 + \text{CP}_4$) and relative importance of intramolecular reactions (upper graph; f_{intra}); **c** application for Diels-Alder based case (network chemistry 3; initial and model parameters: Supplementary Table 3). Relation of stoichiometry for initial building blocks for synthesis at 353 K and simulated number average of CP's with at least 3 crosslinks (black; left axis) and the number average molecular pore size (blue; left axis) at final yield to understand experimental swelling data (orange; right axis; this work; toluene; Supplementary Figure 32a-b). Left part in a-c: 3D visualization at synthesis end (in (a/c) initial molar ratio: 4/2); representative number of molecules highlighting main loops (full connectivity for one molecule in Supplementary Figure 22a); 10% error bar.

Hence, by accessing the contribution of specific molecules either with a given number of CP's of a certain type or a certain level of intramolecular defects we can understand the traditional variation of the storage modulus in Fig. 4b from the molecular scale onwards. The current work thus opens the pathway to control the contribution of specific molecules to the overall macroscopic behavior in this case material stiffness.

In Fig. 4c (right part), we further relate molecular scale information to the swelling degree, which is a key conventional polymer network macroscopic property in the fields of hydrogels and drug delivery.⁴² We focus on previously established rapidly linking ambient temperature Diels-Alder chemistry by the Barner-Kowollik group^{43,44} (chemistry 3) at 353 K and final yield. The initial conditions and parameters are given in Supplementary Table 3 and the model validation in Supplementary Figure 14, selecting tetrafunctional and bifunctional monomeric building blocks. The swelling degree refers to the relative amount of toluene that the network can incorporate compared to the dry gel. The CP distribution, the dangling chain distribution and the molecular pore size distribution from Supplementary Figure 23 are employed to accurately calculate average molecular descriptors. It follows from Fig. 4c (right part) that the further away the initial conditions are from the ideal stoichiometric conditions (molar ratio of 2) the more swelling is observed. Under such premise the simulated average number of CP_x ($x \geq 3$; left axis in right part of Fig. 4c; black symbols) becomes lower and the network structure is more open. More dangling (unreacted) chains remain and the simulated number average molecular pore size increases (left axis; blue symbols), explaining the larger swelling.

Moreover, the left part of Fig. 4c shows the 3D structural incorporation of OH groups as originally present in the bifunctional monomeric building blocks (colored in purple; molar ratio of 2). Such groups are a readily accessible handle for chemical modification (e.g. drug loading) but we cannot assume that they are characterized by a controlled functional group distance distribution, which is a typical assumption if one cannot make a dedicated link to the prior synthesis on the individual functional group level. As shown in Fig. 5a, for the idealized case of $f_{\text{intra}} = 0$ (open purple symbols; molar ratio of 2; additional simulation results in Supplementary Figure 24), a broad OH group distance distribution results representing a wide variety of network molecules. In practice, as only accessible with our

framework, intramolecular reactions occur leading to loop formation so that the OH group distance distribution becomes more complex with a shift to the left and a switch to a bimodal behavior (full purple symbols in Fig. 5a).

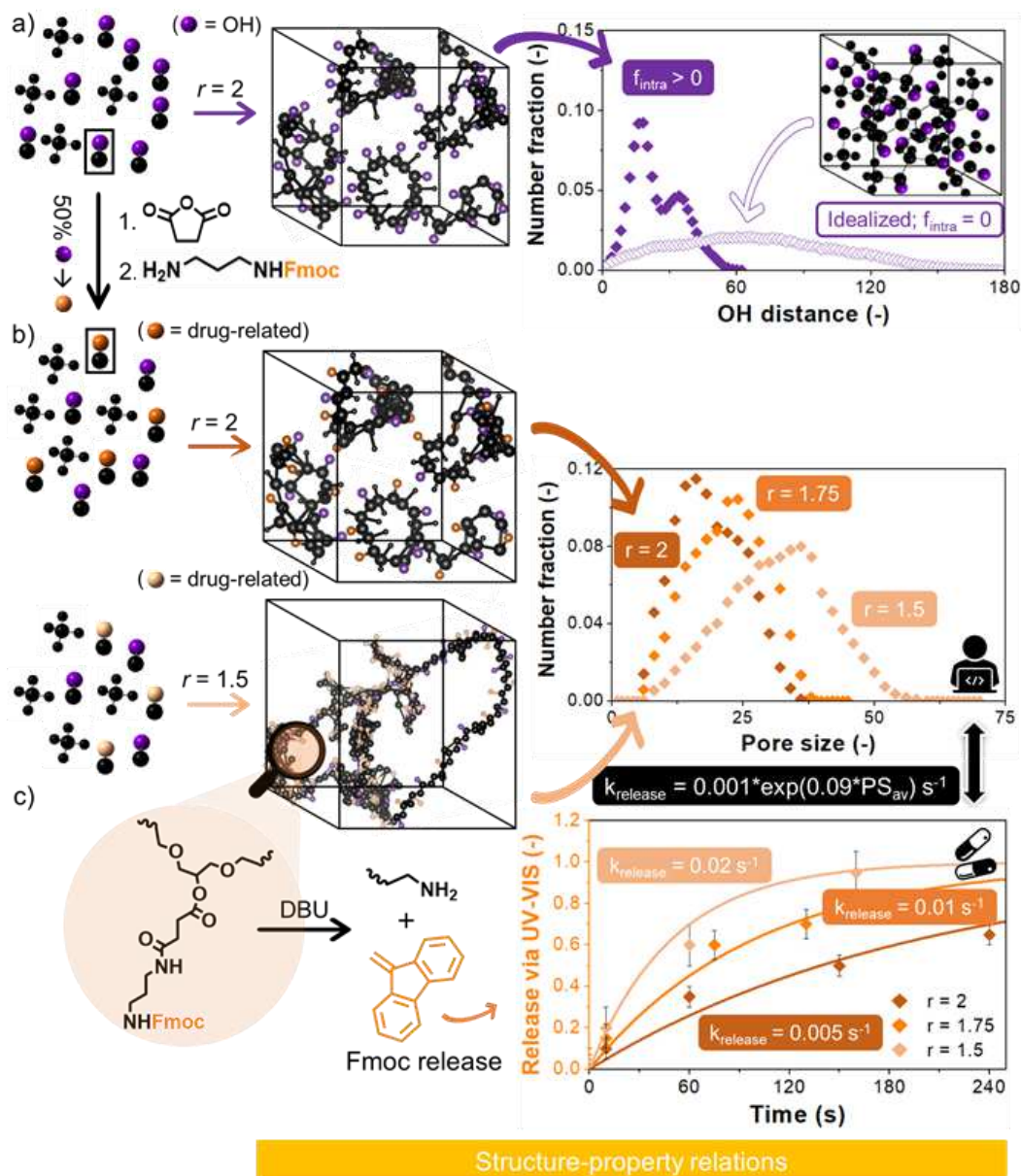


Fig. 5: Relevance of non-idealities for three-dimensional (3D) Diels-Alder based network structures (chemistry 3) at final yield. **a** 3D representation from Fig. 4c (molar ratio r of 2) compared with its ideal counterpart with no intramolecular defects ($f_{\text{intra}}=0$), showing a more complex variation of the OH group distance distribution (full vs. open purple symbols). **b** 3D structure if 50% of the OH groups are replaced by the drug-related tracer Fmoc (Methods section; chemical modification of OH bifunctional linker) for r equal to 2 and 1.5 alongside the molecular pore size distributions, also including the result for $r = 1.75$. **c** Fmoc release curves for r values of 2, 1.5 and 1.75 upon addition of diazabicyclo[5.4.0]undec-7-ene (DBU) considering experimental data in Supplementary Figure 33. Simulated lines are based on release rate coefficients (k_{release} values) that are correlated with the average molecular pore size (PS_{av}) as explicitly calculated from the complete distribution; Fmoc: 3-bis(((2E,4E)-hexa-2,4-dien-1-yl)oxy)propan-2-yl-4-((3-(((9H-fluoren-9yl)methoxy)carbonyl)amino)propyl)amino)-4-oxobutanoate; 10% error bar.

This different 3D spatial arrangement with loop formation affects the material performance, as illustrated in Fig. 5b-c where the Diels-Alder network synthesis is performed under equimolar and non-equimolar conditions (molar ratio of 2, 1.75 and 1.5) with 50% of the bifunctional monomer chemically modified by a tracer representing drug potential (50% replacement of OH (purple) by Fmoc (orange)). Upon measuring the Fmoc release by 1,8-diazabicyclo[5.4.0]undec-7-ene (DBU) attack according to the procedure in the Methods section, it follows that under equimolar conditions the slowest release is obtained (dark orange line in Fig 5c). The corresponding 3D initial structure has the lowest average pore size of 16 units with on average 5 thus a low number of dangling chains so that a slow network modification results. For the non-equimolar case, the average pore size is much larger consistent with a much more open 3D structure depicted. This explains the observation of a faster Fmoc release in Fig. 5c (light orange line), which can be captured by correlating the release rate coefficient $k_{release}$ (s^{-1}) with the average molecular pore size (PS_{av}) calculated from the explicit molecular pore size distribution, as also shown in Fig. 5b-c. In other words, the current platform can be utilized to design molecular pore size distributions toward a controlled drug release behavior by tuning its molecular build-up and regulating molecular scale interactions and 3D space, taking into account the competition of inter- and intramolecular reactions.

Outlook

Our framework provides a detailed characterization and design of both organic and inorganic polymer network materials from the molecular to the application level. We can truly evaluate if a certain network synthesis is close to the targeted structure or not, and we can run the platform over a wide range of reaction conditions to identify the suited reaction conditions, which is purely experimental extremely cost-intensive. The current work also highlights that we need to revise previously developed theories based on average characteristics not explicitly coming from distributions and ideal network representations, as network molecular species are too heterogenous in composition and structure to be described by a single ideal or average molecule.

We can thus perform analysis at the functional group level, which is relevant for existing synthesis platforms but also emerging fields, for instance network materials from supramolecular chemistry in

which it can be expected that only guest-host interactions for individual well-positioned functional groups lead to advanced sensing and molecular recognition.^{45,46} Another example are the more recently developed dynamic recyclable networks in which material reshaping can be fully designed if one knows at which 3D position the exchangeable functional groups are located.^{47,48} In general, based on any desired molecular distributed descriptor, we are capable to fundamentally understand which type of molecules or structural elements allow to design which material property.

Methods

Experimental framework

To illustrate the generic character of the developed framework focus is on three network chemistries: (i) organosilica network synthesis (chemistry 1), epoxy-amine curing (chemistry 2), and Diels-Alder network formation (chemistry 3). As explained below for chemistry 1 literature data were employed and for chemistry 2 and 3 experimental data were recorded in the present work.

For chemistry 1, tetraethylorthosilicate (TEOS) is used as the organosilica precursor, considering literature data³⁷ at 298 K on both the synthesis and the characterization. The initial mixture consists of 0.022 L TEOS, 0.0072 L H₂O (pH = 2.5), and 0.022 L ethanol (EtOH) in a molar ratio 1:4:3.8 with hydrogen chloride (HCl) as catalyst. By selecting a pH of 2.5 near the isoelectric point of the silica sol, hydrolysis and condensation steps can be partially separated and elegantly studied by ²⁹Si nuclear magnetic resonance (NMR), facilitating parameter tuning of the associated k_{chem} values. The NMR spectra were recorded by Pouxviel et al.³⁷ at 298 K and 80 MHz employing an AM400 wide bore Bruker spectrometer. After preparation the sols were directly placed in NMR tubes. The acquisition time was 0.5 s and a relaxation delay of 5 s was used. Exponential multiplication was applied before Fourier transformation. The experimental data are provided as symbols in Fig. 3 and Supplementary Figure 11 and 12, with the parameter tuning procedure based on these data highlighted in the Supplementary discussion and the optimized parameters listed in Supplementary Table 1. A distinction is made here between parameter tuning at smaller times (Supplementary Figure 11) and larger times (Supplementary Figure 12).

For chemistry 2, bisphenol-F diglycidyl ether (DGEBF; Sigma-Aldrich, used as received) and ethylene diamine (EDA; Sigma-Aldrich, used as received) were used as precursors to perform the epoxy-amine curing at 298 K. The curing was analyzed with near-infrared (nIR) spectroscopy employing an in-house available Perkin Elmer Lambda 900 UV/VIS/NIR Spectrometer. Both the DGEBF and EDA precursor were thoroughly mixed with equimolar functional group concentrations before being brought into a nIR-transparent cuvette. nIR spectra of the reaction mixture were subsequently recorded at frequent time intervals from 4000 to 10000 cm^{-1} with a resolution of 3 nm. The concentration of primary, secondary and tertiary amine, epoxide and hydroxyl groups were analyzed as a function of synthesis time using Spectragryph software, according to the procedure previously reported.⁴⁹ In this procedure, the spectra are internally normalized by the aromatic ring peak at 4620 cm^{-1} and then the primary amine and epoxide concentration are determined by integration of the peaks at 4925 and 4520 cm^{-1} . Based on these concentration profiles, the three major reactions from Supplementary Figure 6 could be followed upon using a mass balance approach⁴⁹ with the kinetic results given in Supplementary Figure 13a.

The mechanical response variation more specifically the variation of the (storage) modulus as a function of synthesis time, as needed for the construction of Fig. 5b, was recorded using a Dynamic Mechanical Analyzer (DMA Q800, TA Instruments) at room temperature, considering a precursor mixture with equimolar FGs as brought in a flexible cuvette that was tested under three point bending with following settings: 1 Hz, 30 μm amplitude, and 15 mm span. Due to the flexible cuvette necessary to carry the reaction mixture during DMA analysis, an initial storage modulus of 20 MPa is obtained thus for the unreacted resin (see double orange arrow in Fig. 5b). As the sample holder remains the same during the experiment, there is no further influence on the curve trend.

For chemistry 3, a small molecule experiment (Supplementary Figure 14; phase 3a) with monofunctional reactants representing the functional groups of the multifunctional monomeric building blocks for the actual Diels-Alder network formation (Supplementary Figure 7) has been first conducted. Phase 3b then consists of the actual network formation (use of OH-based bifunctional linker) and Phase 3c to a similar network formation but with drug release capacities (partial use of Fmoc-modified bifunctional linker; Fmoc is fully known as 1,3-bis(((2E,4E)-hexa-2,4-dien-1-yl)oxy)propan-2-yl-4-((3-(((9H-fluoren-9-

yl)methoxy)carbonyl)amino)propyl)amino)-4-oxobutanoate)). In what follows, after a discussion of the analysis techniques, the synthesis details of the small molecule experiment are given and then the synthesis details of the network formations are provided. Unless stated otherwise, all chemicals and solvents were used as received from the supplier without further purification.

^1H - and ^{13}C -NMR spectra were recorded on a Bruker System 600 Ascend LH, equipped with a BBO-Probe (5 mm) with z-gradient (^1H : 600.13 MHz; ^{13}C : 150.90 MHz,). All measurements were carried out in deuterated solvents (Supplementary Figure 26-29). Resonances were recorded in parts per million (ppm) relative to tetramethylsilane (TMS). The δ -scale was calibrated to the respective residual solvent signal. The measured coupling constants were calculated in Hz. To analyze the spectra the software MESTRENOVA 11.0 was used. The signals were quoted as s = singlet, bs = broad singlet, d = doublet, t = triplet, dd = doublet of doublets, and m = multiplet.

Liquid chromatography – electrospray ionization – high resolution mass spectroscopy (LC-ESI-HRMS) measurements (Supplementary Figure 30-31) were additionally performed considering an UltiMate 3000 UHPLC system (Dionex, Sunnyvale, CA, USA) consisting of a pump (LPG 3400SZ, autosampler WPS 3000TSL) and a temperature-controlled column department (TCC 3000). Separation was performed on a C18 HPLC-column (Phenomenex Luna 5 μm , 100 Å, 250 \times 2.0 mm) operating at 313 K. A gradient of acetonitrile:water 10:90 to 80:20 v/v (additive 10 mmol L $^{-1}$ ammonium acetate, acetonitrile: Thermo Fisher Scientific, after drying and purification with SP-1 Stand Alone Solvent Purification System LC Technology Solutions Inc) at a flow rate of 0.20 mL min $^{-1}$ was used during 15 min as the eluting solvent. The flow was split in a 9:1 ratio with 90% (0.18 mL min $^{-1}$) of the eluent directed through the UV-detector (VWD 3400, Dionex, detector wavelengths 215, 254, 280, 360 nm) and 10 % (0.02 mL min $^{-1}$) infused into the electrospray source. Spectra were recorded on a LTQ Orbitrap Elite mass spectrometer (Thermo Fisher Scientific, San Jose, CA, USA) equipped with a HESI II probe. The instrument was calibrated in the m/z range 74-1822 using premixed calibration solutions (Thermo Scientific). A constant spray voltage of 3.5 kV, and a dimensionless sheath gas and a dimensionless auxiliary gas flow rate of 5 and 2 were applied. The capillary temperature was set to 573 K, the S-lens RF level to 68, and the aux gas heater temperature to 598 K.

Trans, trans-hexa-2,4-dienol (sorbic alcohol, reactant 1 in small molecule experiment; phase 3a) was synthesized by adding sorbic acid (1.00 g, 8.92 mmol, 1 eq.; Sigma-Aldrich) dissolved in 50 mL diethyl ether (Et₂O; Thermo Fisher Scientific) dropwise to a 250 mL round bottom flask with lithium aluminium hydride (LiAlH₄; 0.94 g, 26.76 mmol, 3 eq.; 95%; Sigma-Aldrich) and 25 mL diethyl ether (Supplementary Figure 25; reaction (1)). A reflux condenser was installed and the aperture was purged with argon. After addition, the reaction was stirred at ambient temperature for 15 min and then refluxed for 1 h. The residual lithium aluminium hydride was subsequently quenched with the addition of isopropanol (Thermo Fisher Scientific), then water, following by vacuum filtration. The liquid was subsequently extracted twice with water (20 mL), dried over magnesium sulphate and the solvent removed under reduced pressure. Flash column chromatography (10:90 to 30:70 ethyl acetate:hexane) yielded the pure product as a colorless oil which crystalized over time (0.610 g, 6.30 mmol, 70% yield); specifications: ¹H-NMR (600 MHz, CDCl₃); δ (¹H) = 6.24 – 6.17 (m, 1H, CH-2), 6.10 – 6.03 (m, 1H, CH-3), 5.71 (tdt, *J* = 9.1, 6.7, 4.4 Hz, 2H, CH-4,5), 4.17 – 4.13 (m, 2H, CH₂-1), 1.76 (d, *J* = 6.4 Hz, 3H, CH₃-6) (Supplementary Figure 26a).

Methyl 4-(((diethoxyphosphoryl)carbonothioyl)-thio)methyl)benzoate (RAFT agent; reactant 2 in small molecule experiment; phase 3a) was prepared according the following procedure. In a two-necked 50 mL round bottom flask, equipped with a reflux condenser and a magnetic stirrer, sodium hydride (0.235 g, 9.78 mmol, 1 eq.; 60% suspension in paraffin oil; Sigma-Aldrich) and dry tetrahydrofuran (THF; 5 mL; Thermo Fisher Scientific, after drying and purification with SP-1 Stand Alone Solvent Purification System LC Technology Solutions Inc.) were added. To that suspension a solution of diethyl phosphite (1.35 g, 9.78 mmol, 1 eq.; Sigma-Aldrich) in THF (5 mL) was added dropwise. The mixture was subsequently heated to reflux for 5 minutes. Afterwards, the reaction mixture was cooled in an ethyl acetate-liquid nitrogen bath and C₂S (3.72 g, 47.87 mmol, 5 eq.; Sigma-Aldrich) was added. Methyl 4-(bromomethyl)benzoate (2.46 g, 10.75 mmol, 1.1 eq.; Sigma-Aldrich) was then added dropwise to the reaction mixture and stirred for 2 h (Supplementary Figure 25; reaction (3)). Hexane was added (30 mL; Thermo Fisher Scientific), the mixture filtered and the solvent removed under vacuum conditions. The pure product (2.3 g, 6.4 mmol, 65% yield) was obtained after passing over a short silica column using first cyclohexane and then diethyl ether; specifications: ¹H-NMR (600 MHz, Toluene-*d*₈); δ (¹H) = 7.90

– 7.84 (m, 2H, CH-2,6), 6.85 – 6.80 (m, 2H, CH-3,5), 4.13 – 3.99 (m, 4H, CH₂-8), 3.97 (s, 2H, CH₂-7), 3.53 – 3.47 (m, 3H, CH₂-10), 1.05 (td, *J* = 7.1, 0.7 Hz, 6H, CH₂-9) (Supplementary Figure 27a). LC-ESI-HRMS (*m/z*) calculated for [C₁₄H₁₉O₅PS₂H]⁺: 363.0484, measured: 363.0495 (Supplementary Figure 30b).

For the small molecule experiment, sorbic alcohol (reactant 1; 0.549 mg, 1 eq.) and the RAFT agent (reactant 2; 2.02 mg, 1 eq.) were dissolved in toluene (0.5 mL; Thermo Fisher Scientific, after drying and purification with SP-1 Stand Alone Solvent Purification System LC Technology Solutions Inc.). The vial was closed and purged with a constant argon flow for 5 minutes. The reaction mixture was heated up to 353 K and maintained at that temperature. Conversion was determined using ¹H NMR spectroscopy (600 MHz; chloroform-*d*₃, Sigma-Aldrich).

Network formation (phase 3b) was subsequently performed considering a tetrafunctional and bifunctional monomeric building block related to phase 3a, respectively denoted as reactant 3 and reactant 4. Benzene-1,2,4,5-tetrayltetrakis(methylene)tetrakis((diethoxyphosphoryl)-methanedithioate) (reactant 3: tetrafunctional monomer) was synthesized as follows. In a dry 10 mL Schlenk tube with a magnetic stirrer, sodium hydride (suspension in paraffin oil; 90.0 mg, 1.74 mmol, 1 eq.; Sigma-Aldrich) was added and vigorously mixed with 3 mL heptane (Thermo Fisher Scientific). After a few minutes, the liquid phase was removed and heptane was added again. The procedure was repeated three times until a white powder of sodium hydride was obtained. The residual liquid was removed under vacuum conditions and dry THF (2 mL) was added. To that suspension a solution of diethyl phosphite (240 mg, 1.74 mmol, 1 eq.; Sigma-Aldrich) in THF (1 mL) was added dropwise. After addition, the mixture was allowed to stir for 1 h and then heated to 339 K for 2 minutes. After cooling the reaction mixture in an acetone-liquid nitrogen bath, CS₂ (660 mg, 8.70 mmol, 5 eq.; Sigma-Aldrich) was added over a period of 1 h followed by additional stirring at ambient temperature. The reaction mixture was cooled again to 273 K and 1,2,4,5-tetrakis(bromomethyl)-benzene (195 mg, 0.42 mmol, 0.25 eq.; Sigma-Aldrich) dissolved in 1 mL dry THF was added dropwise (Supplementary Figure 25; reaction (4)). After completion, the reaction mixture was stirred for another hour, followed by solvent removal under vacuum conditions. The pure product (260 mg, 0.26 mmol, 62% yield) was obtained after flash column chromatography (100:0 to 98:2 dichloromethane:methanol); specifications: ¹H-NMR (600 MHz,

DMSO-*d*₆) δ (¹H) = 7.53 (s, 2H, CH-3,6), 4.56 (s, 8H CH₂-7), 4.15 (dq, *J* = 8.6, 7.0, 5.3 Hz, 16H, CH₂-8), 1.25 (s, 24H, CH₃-9) (Supplementary Figure 27b). LC-ESI-HRMS (*m/z*) calculated for [C₃₀H₅₀O₁₂P₄S₈H]⁺: 983.0091, measured: 983.0079 (Supplementary Figure 30c).

1,3-Bis(((2E,4E)-hexa-2,4-dien-1-yl)oxy)propan-2-ol (reactant 4: bifunctional monomer; phase 3b) was synthesized starting from sorbic alcohol. Sorbic alcohol (848 mg, 8.65 mmol, 4 eq.) and epichlorohydrin (200 mg, 2.16 mmol, 1 eq.; Sigma-Aldrich) were placed in a 25 mL round bottom flask, equipped with a stir bar and purged with argon. To this solution, potassium hydroxide (KOH; 363 mg, 6.48 mmol, 3 eq.; Thermo Fisher Scientific) and tetrabutylammonium iodine (Bu₄NI; 160 mg, 0.43 mmol, 0.2 eq.; 98%, Sigma-Aldrich) were added (Supplementary Figure 25; reaction (2)). The reaction mixture was stirred over a period of 48 h at 338 K. After cooling to ambient temperature, the obtained slurry was dissolved in dichloromethane (DCM; 20 mL; Thermo Fisher Scientific, after drying and purification with SP-1 Stand Alone Solvent Purification System LC Technology Solutions Inc.) and extracted with water (20 mL), followed by evaporation under reduced pressure. After flash column chromatography (93:7 to 70:30 ethyl acetate:hexane) the product was obtained as a colorless viscous oil (0.34 g, 1.34 mmol, 62% yield); specifications: ¹H-NMR (600 MHz, CDCl₃) δ (¹H) = 6.23 – 6.16 (m, 2H, CH-5), 6.09 – 6.02 (m, 2H, CH-4), 5.71 (dq, *J* = 13.6, 6.7 Hz, 2H, CH-3), 5.61 (dtq, *J* = 14.3, 6.3, 0.7 Hz, 2H, CH-2), 4.05 – 4.00 (m, 4H, CH₂-7), 3.96 (tq, *J* = 6.4, 4.3 Hz, 1H, CH-8), 3.50 (dd, *J* = 9.7, 4.4 Hz, 2H, CH₂-1), 3.44 (dd, *J* = 9.7, 6.4 Hz, 2H, CH₂-1), 2.44 (d, *J* = 4.1 Hz, 1H, OH), 1.76 (dd, *J* = 6.8, 1.6 Hz, 6H, CH₃-6) (Supplementary Figure 26b); ¹³C-NMR (151 MHz, CDCl₃) δ (¹³C) = 133.59 (C-3), 130.83 (C-4), 130.33 (C-5), 126.45 (C-2), 71.89 (C-1), 71.21 (C-8), 69.67 (C-7), 18.19 (C-6) (Supplementary Figure 26c). LC-ESI-HRMS (*m/z*) calculated for [C₁₅H₂₄ONa]⁺: 275.1617, measured: 275.1610 (Supplementary Figure 30a).

For network formation, tetrafunctional monomer (reactant 3; 26.5 mg, 0.027 mmol, 1 eq.), different equivalents of bifunctional monomer (reactant 4; 6.8 mg, 1 eq.; 10.2 mg, 1.5 eq.; 11.9 mg, 1.75 eq.; 13.6 mg, 2 eq.) and toluene (0.025 mL) were added in a 1 mL crimp vial. The vial was closed and purged with a constant argon flow for 5 minutes. Afterwards, the reaction mixture was heated up to 353 K for 24 h and analysis was performed. The networks did not dissolve in toluene and swelling tests were done

in that solvent for 3 h. The percentual degree of swelling was calculated according to the ratio of 100 ($w_s - w_d$) and w_d , with w_s the mass of the sample after 3 h swelling and w_d the mass of sample prior to swelling. The related experimental data are included in Fig. 4c. Images of the synthesized networks are shown in Supplementary Figure 32a (before swelling) and Supplementary Figure 32b (after addition of toluene). A clear difference in color can be seen depending on the initial ratio of the two monomers. Under stoichiometric conditions a yellow network is obtained, while going more and more to off-stoichiometric conditions (excess of tetrafunctional linker) a pink color is observed due to the presence of unreacted dithioester moieties of the tetrafunctional linker.

Moreover, in phase 3c, the network synthesis was also performed with Fmoc-loaded bifunctional monomer (reactant 5; short notation bifunctional linker-Fmoc, with the main results shown in Figure 5. This monomer was synthesized by chemically modifying reactant 4 (shortly bifunctional linker-OH) in two steps (Supplementary Figure 25 reaction (5) as step 1 and reaction (6) as step 2). In step 1, sodium hydride (60% suspension in oil; 20.9 mg, 0.87 mmol, 1.1 eq.) was placed into a dry 25 mL Schlenk flask and suspended in 5 mL anhydrous THF. Under vigorous stirring reactant 3 (200.0 mg, 0.792 mmol, 1.0 eq.), solved in 3 mL THF, was added dropwise. Upon completion, the reaction mixture was allowed to stir for one additional hour at room temperature, followed by refluxing the suspension for 5 min. The reaction mixture was broad back to room temperature and succinic anhydride (87.2 mg, 0.872 mmol, 1.1 eq.; Sigma Aldrich), solved in 2 mL THF, was added dropwise. After additional stirring overnight, the solvent was removed in vacuum and the mixture evaporated onto celite. The step 1 product (shortly bifunctional linker-COOH; 0.19 g, 0.50 mmol, 63% yield) was obtained as a colorless viscous oil after flash column chromatography (90:10 to 50:50 ethyl acetate:cyclohexane with 1% formic acid); specifications: $^1\text{H-NMR}$ (600 MHz, CDCl_3) δ (^1H) = 6.21 – 6.14 (m, 2H), 6.05 (ddq, $J = 14.1, 10.5, 1.7$ Hz, 2H), 5.71 (dq, $J = 13.7, 6.7$ Hz, 2H), 5.61 – 5.54 (m, 2H), 5.14 (t, $J = 5.0$ Hz, ^1H), 4.00 (h, $J = 6.3$ Hz, 4H), 3.62 – 3.53 (m, 4H), 2.71 – 2.63 (m, 4H), 1.75 (dd, $J = 6.8, 1.6$ Hz, 6H) (Supplementary Figure 28a); $^{13}\text{C-NMR}$ (151 MHz, CDCl_3) δ (^{13}C) = 176.89, 171.86, 133.61, 130.89, 130.38, 126.44, 72.29, 71.86, 68.42, 29.20, 28.94, 18.25 (Supplementary Figure 28b). LC-ESI-HRMS (m/z) calculated for $[\text{C}_{20}\text{H}_{29}\text{O}_7]$: 351.1802 measured: 351.1819 (Supplementary Figure 31a).

In step 2, in a dry 10 mL Schlenk flask bifunctional linker-COOH (100 mg, 0.26 mmol, 1.0 eq.), N-Fmoc-1,3-propanediamine hydrobromide (96 mg, 0.29 mmol, 1.1 eq. Combi-Blocks), N,N'-dicyclohexylcarbodiimide (DCC; 70 mg, 0.34 mmol, 1.3 eq.; Sigma Aldrich), and 4-dimethylaminopyridine (DMAP; 3 mg, 0.03 mmol, 0.1 eq.; Sigma Aldrich) were placed and solved in 1.5 mL dry dimethylformamide (DMF; Sigma Aldrich). After short stirring N,N-diisopropylethylamine (DIPEA; 50 μ L, 0.28 mmol, 1.0 eq.; Sigma Aldrich) was added and the reaction mixture was stirred for 3 h at room temperature. Upon completion, the solvent was removed under high vacuum without applying heat. The crude reaction mixture was evaporated onto celite and purified by flash column chromatography (100:0 to 50:50 ethyl acetate:cyclohexane) to obtain bifunctional linker-Fmoc, thus reactant 5 (55 mg, 0.08 mmol, 32% yield); specifications: $^1\text{H-NMR}$ (600 MHz, CDCl_3) δ (^1H) = 7.89 (d, J = 7.6 Hz, 2H), 7.87 – 7.81 (m, ^1H), 7.68 (d, J = 7.5 Hz, 2H), 7.45 – 7.39 (m, 2H), 7.34 (dtd, J = 11.2, 7.4, 1.1 Hz, 2H), 7.24 (t, J = 5.8 Hz, 1H), 6.22 – 6.13 (m, 2H), 6.10 – 6.02 (m, 2H), 5.70 (dp, J = 13.8, 6.9 Hz, 2H), 5.57 (dt, J = 15.5, 6.4 Hz, 2H), 4.98 (p, J = 5.1 Hz, 1H), 4.30 (dd, J = 7.0, 2.4 Hz, 2H), 4.21 (t, J = 7.0 Hz, 1H), 3.95 (q, J = 5.7 Hz, 4H), 3.46 (d, J = 5.2 Hz, 4H), 3.01 (dp, J = 26.5, 6.8 Hz, 4H), 2.37 – 2.31 (m, 2H), 1.72 (td, J = 6.8, 1.9 Hz, 6H) (Supplementary Figure 29a); $^{13}\text{C-NMR}$ (151 MHz, CDCl_3) δ (^{13}C) = 171.93, 156.63, 142.57, 139.42, 137.43, 132.46, 130.87, 129.55, 128.94, 127.30, 126.99, 121.40, 120.04, 109.78, 71.39, 70.65, 67.94, 33.35, 29.89, 29.70, 29.20, 25.33, 24.47, 17.88 (Supplementary Figure 29b). LC-ESI-HRMS (m/z) Calculated for $[\text{C}_{37}\text{H}_{46}\text{N}_2\text{O}_7\text{H}]^+$: 631.3378 measured: 631.3378, $[\text{C}_{37}\text{H}_{46}\text{N}_2\text{O}_7\text{Na}]^+$: 653.3197 measured: 653.3171, $[\text{C}_{37}\text{H}_{46}\text{N}_2\text{O}_7\text{K}]^+$: 669.2973 measured: 669.2903 (Supplementary Figure 31b).

The subsequent network synthesis was performed in a 1 mL crimp vial adding reactant 3 (21.0 mg, 0.022 mmol, 1.00 eq.), different equivalents of reactant 5 always obeying a 1:1 molar mixture of functionalized (bifunctional linker-Fmoc) to unfunctionalized bifunctional linker being reactant 4 (bifunctional linker-OH) (14.1 mg/6.0 mg, 2.00 eq.; 12.7 mg/5.4 mg, 1.75 eq.; 10.8 mg/4.7 mg, 1.5 eq.), and toluene (0.020 mL). The vial was closed and purged with a constant argon flow for 5 min. Afterwards, the reaction mixture was heated over 24 h at 353 K. The generated networks were removed and used for analysis.

Images of the synthesized networks with the difference in color depending on the initial monomer ratio are shown in Supplementary Figure 32c.

The Fmoc (drug proxy) release was undertaken in UltraViolet-Visible (UV/Vis) cuvettes (Supplementary Figure 33). The respective network ($r = 2$; 1.3 mg or $r = 1.75$; 1.5 mg or $r = 1.5$; 3.2 mg) was added into the cuvette and washed with DMF (three times). Afterwards, the cleavage solution (2 mL; 2% 1,8-diazabicyclo[5.4.0]undec-7-ene (DBU; Sigma Aldrich) in DMF) was added, the cuvette was inverted twice to ensure homogenic mixing and the UV-Vis spectrum was immediately measured (first measurement after ca. 10 s). This was repeated until the final measuring time was reached.

Modeling framework

As conceptually illustrated in Fig. 2 and highlighted in detail by interactive flowsheets as defined by Supplementary Figure 1-3 matrix-based kinetic Monte Carlo (*kMC*) simulations are combined in the present work with molecular dynamic (MD) simulations to follow the kinetics and 3D incorporation of each building block or functional group as a function of synthesis time t . In the Supplementary methods section, a dedicated explanation of each technical implementation characteristic in these flowsheets is given by introducing boxes with labels from A to N and providing a detailed discussion of the key implementation steps for each of these boxes.

In this subsection, the essential information for the most critical implementation characteristics of the interactive flowsheets is provided to enable a general reader to grasp the overall technical innovation. In the core matrix-based *kMC* simulations, reaction event per reaction event is sampled based on reaction probabilities as represented by means of a cumulative probability curve, starting from a sufficiently large number of initial molecules to ensure numerical convergence as shown in Supplementary Figure 16 for chemistry 1 selecting some key molecular characteristics. The update of the reaction probabilities after the occurrence of a reaction event requires the discrete updates of the reaction rates, which are directly related to (i) the chemistry platform selected defining the potential reaction types between the functional groups present and (ii) the reaction mixture composition defining the (reactant) concentrations related to these reaction types.

So-called apparent rate coefficients (k_{app} values) are considered for the calculation of the MC reaction probabilities to acknowledge that the observed reactivities for intermolecular reactions can be influenced by both intrinsic chemical reactivities (need of Arrhenius parameters for the calculation of chemical rate coefficients, i.e. k_{chem} values) and (chain length and CP dependent) diffusivities (need of diffusion coefficients for the calculation of diffusion rate coefficients, i.e. k_{diff} values). For an intramolecular reaction the interplay of chemistry and diffusivity is also addressed by the application of a fundamental distance rule to verify if the functional groups involved can react due to a sufficient flexibility of the associated network molecule. The relevance of these diffusional limitations is highlighted in Supplementary Figure 18 and 19, considering chemistry 1.

If as a consequence of an executed reaction event a network segment or dangling chain is formed, a composite topology matrix T is updated in the $k\text{MC}$ algorithm. This composite matrix stores (i) the compositions of all individual segments and dangling chains in a core topology matrix and (ii) the associated network connectivities in 2 additional connectivity arrays embedding thus coupling this core matrix. At predetermined thus user-defined plotting times the composite topology matrix can be used to obtain the visualization of individual (network) molecules in 2D or 3D format. For the latter format every row in the composite topology matrix is scanned and the associated bond length, bond angles, and dihedral angles are sampled based on cumulative probability distributions that are ideally constructed based on MD simulations.

In the present work, most simulation emphasis is on the organosilica network synthesis case (Fig. 3 and Fig. 4a) for which Burg et al.¹⁰ applied the MD Large-scale Atomic/Molecular Massively Parallel Simulator (LAMMPS; Supplementary Figure 3a), with post-processing allowing the calculation of the equilibrium distributions of bond lengths and angles. Corrections are introduced if no MD data are available, which is e.g. the case if a structural defect is encountered that has been created due to a chemical reaction omitted in typical MD simulations, as illustrated for the organosilica case in Supplementary Table 5.

Due to the discrete nature of the developed modeling framework we can select the simulation times when we want to switch to the more detailed part regarding molecular specifications and configurations. The more frequently this switch is performed the more detailed the modeling outcome becomes albeit

at computational cost. The need for a switch is directly related to the overall kinetics as for instance deducible from the yield profile with a steep variation implying strongly alternating kinetics. In the present work, we have carefully analyzed the switching times to guarantee numerical convergence and sufficient molecular detail on the one hand and an acceptable computational cost on the other hand. For defect free structures, using supercomputer platforms as in the present work, we have a couple of hours as simulation time. With more structural defects formed the simulation time increases and we have with current supercomputer capacities a simulation time of a few days. Of course the MD input data need to be acquired as well and there we have simulation times on the scale of hours, days or weeks depending on the required potential field.

To highlight the general accuracy of the developed modeling framework we showcase in Supplementary Figure 17 a successful benchmark for chain length distributions considering the work of Flory, who extended the work of Stockmayer.⁵⁰ Our simulated distributions are consistent with their analytical equations upon simplifying our framework with their assumptions of equal reactivity for functional groups and the absence of intramolecular reactions. We focus on the results for network chemistry 1.

The novelty of the modeling framework is also clear from the overview of experimental and theoretical methodologies as reported in the last decades, as listed in Supplementary Figure 15 also including ca. 100 references to fully place the current work in context of the state-of-the-art. Experimentally one cannot access the molecular scale for a general chemistry and theoretically one either has no real network material due to focus on too low synthesis times or an idealized high yield network material with focus on high synthesis times without covering the competition of inter- and intramolecular reactions and the interplay of chemistry and diffusional limitations. Specifically so-called conditional Monte Carlo methods have been developed in which predefined distributions are utilized to sample molecular scale phenomena. However, as clear for the results of the three cases studied in the present work, distributed molecular descriptors (e.g. the dangling and crosslinking point distribution) are very dynamic as a function of synthesis time and thus a general shape cannot be introduced a priori. Instead reaction event driven coupled matrix-based *k*MC simulations are needed in which connectivity by connectivity is tracked covering both the formation of ideal and non-ideal structural elements.

In addition, in the Supplementary Discussion, all the required steps for the determination of the chemical and diffusional limitations related input parameters are covered for each chemistry. A general research strategy is followed in which smaller synthesis times or reaction systems with monofunctional analogues are considered to determine chemistry related kinetic parameters free from the impact of diffusional limitations. The larger synthesis times are subsequently employed to tune diffusional limitations related parameters with as input the previously determined chemistry related kinetic parameters. Hence, inherently parameter correlation is minimized also bearing in mind that specific experimental responses or variations within a selected response are considered. This is further illustrated in Supplementary Figure 11-14 with the experimental data represented by symbols and the model outcome with optimized parameters as full lines. Also simplified model descriptions are included as dashed lines with clear deviations for the full lines, highlighting the need of the appropriate tuning of model parameters and the relevance of the generic approach put forward.

Data availability

The authors declare that all data supporting the findings of this study are available within the open literature, this paper and its supplementary information files.

Code availability

The authors declare that the algorithm of the modeling framework is available in the open literature, the paper, and its supplementary information files. All rights are reserved and the source is not released.

References

1. Flory, P. J. Network topology and the theory of rubber elasticity. *Br. Polym. J.* **17**, 96-102 (1985).
2. Kryven, I. Bond percolation in coloured and multiplex networks. *Nat. Commun.* **10**, 404 (2019).
3. Zhong, M. J., Wang, R., Kawamoto, K., Olsen, B. D. & Johnson, J. A. Quantifying the impact of molecular defects on polymer network elasticity. *Science* **353**, 1264-1268 (2016).
4. Sheiko, S. S. & Dobrynin, A. V. Architectural code for rubber elasticity: from supersoft to superfirm materials. *Macromolecules* **52**, 7531-7546 (2019).

5. LLorca, J. On the quest for the strongest materials. *Science* **360**, 264-265 (2018).
6. Berman, D., Erdemir, A. & Sumant, A. V. Graphene: a new emerging lubricant. *Mater. Today* **17**, 31-42 (2014).
7. Anderson, M. W. & Klinowski, J. Direct observation of shape selectivity in zeolite ZSM-5 by magic-angle-spinning NMR. *Nature* **339**, 200-203 (1989).
8. Rimer, J. D. Rational design of zeolite catalysts. *Nat. Catal.* **1**, 488-489 (2018).
9. Boerjan, W., Ralph, J. & Baucher, M. Lignin Biosynthesis. *Annu. Rev. Plant Biol.* **54**, 519-546 (2003).
10. Burg, J. A. & Dauskardt, R. H. Elastic and thermal expansion asymmetry in dense molecular materials. *Nat. Mater.* **15**, 974-980 (2016).
11. Owens, G. J. et al. Sol-gel based materials for biomedical applications. *Prog. Mater Sci.* **77**, 1-79 (2016).
12. Loccufier, E. et al. Silica nanofibrous membranes for the separation of heterogeneous azeotropes. *Adv. Funct. Mater.* **28**, 1804138 (2018).
13. Caló, E. & Khutoryanskiy, V. V. Biomedical applications of hydrogels: a review of patents and commercial products. *Eur. Polym. J.* **65**, 252-267 (2015).
14. D'hooge, D. R., Van Steenberge, P. H. M., Reyniers, M.-F. & Marin, G. B. The strength of multi-scale modeling to unveil the complexity of radical polymerization. *Prog. Polym. Sci.* **58**, 59-89 (2016).
15. Matyjaszewski, K. Advanced materials by atom transfer radical polymerization. *Adv. Mater.* **30**, 1706441 (2018).
16. Van Steenberge, P. H. M. et al. Visualization and design of the functional group distribution during statistical copolymerization. *Nat. Commun.* **10**, 3641 (2019).
17. Di Lorenzo, F. & Seiffert, S. Nanostructural heterogeneity in polymer networks and gels. *Polym. Chem.* **6**, 5515-5528 (2015).
18. Gu, Y., Zhao, J. & Johnson, J. A. Polymer networks: from rubbers and gels to porous frameworks. *Angew. Chem. Int. Edit.* **59**, 5022-5049 (2020).
19. Sandakov, G. I., Smirnov, L. P., Sosikov, A. I., Summanen, K. T. & Volkova, N. N. NMR analysis of distribution of chain lengths between crosslinks of polymer networks. *J. Polym. Sci. Pol. Phys.* **32**, 1585-1592 (1994).

20. Mathur, A. M. & Scranton, A. B. Characterization of hydrogels using nuclear magnetic resonance spectroscopy. *Biomaterials* **17**, 547-557 (1996).
21. Tripathi, A. K., Neenan, M. L., Sundberg, D. C. & Tsavalas, J. G. Influence of n-alkyl ester groups on efficiency of crosslinking for methacrylate monomers copolymerized with EGDMA: experiments and Monte Carlo simulations of reaction kinetics and sol-gel structure. *Polymer* **96**, 130-145 (2016).
22. Kryven, I., Duivenvoorden, J., Hermans, J. & Iedema, P. D. Random graph approach to multifunctional molecular networks. *Macromol. Theor. Simul.* **25**, 449-465 (2016).
23. Fierens, S. K. et al. Model-based design to push the boundaries of sequence control. *Macromolecules* **49**, 9336-9344 (2016).
24. Buback, M., Feldermann, A., Barner-Kowollik, C. & Lacik, I. Propagation rate coefficients of acrylate-methacrylate free-radical bulk copolymerizations. *Macromolecules* **34**, 5439-5448 (2001).
25. Van Steenberge, P. H. M. et al. Linear gradient quality of ATRP copolymers. *Macromolecules* **45**, 8519-8531 (2012).
26. D'hooge, D. R. In silico tracking of individual species accelerating progress in macromolecular engineering and design. *Macromol. Rapid Commun.* **39**, 1800057 (2018).
27. Burg, J. A. et al. Hyperconnected molecular glass network architectures with exceptional elastic properties. *Nat. Commun.* **8**, 1019 (2017).
28. Schwab, F. K. & Denniston, C. Reaction and characterisation of a two-stage thermoset using molecular dynamics. *Polym. Chem.* **10**, 4413-4427 (2019).
29. Zanjani, M. B. et al. Computational investigation of the effect of network architecture on mechanical properties of dynamically cross-linked polymer materials. *Macromol. Theor. Simul.* **28**, 1900008 (2019).
30. Oliver, M. S., Dubois, G., Sherwood, M., Gage, D. M. & Dauskardt, R. H. Molecular origins of the mechanical behavior of hybrid glasses. *Adv. Funct. Mater.* **20**, 2884-2892 (2010).
31. Kilic, K. I. & Dauskardt, R. H. Design of ultrastiff organosilicate hybrid glasses. *Adv. Funct. Mater.* **29**, 1904890 (2019).
32. Talati, M., Albaret, T. & Tanguy, A. Atomistic simulations of elastic and plastic properties in amorphous silicon. *Europhys. Lett.* **86**, 66005 (2009).
33. Kawamoto, K., Zhong, M. J., Wang, R., Olsen, B. D. & Johnson, J. A. Loops versus branch functionality in model click hydrogels. *Macromolecules* **48**, 8980-8988 (2015).

34. Dušek, K. & Patterson, D. Transition in swollen polymer networks induced by intramolecular condensation. *J. Polym. Sci. Pol. Phys.* **6**, 1209-1216 (1968).
35. Panyukov, S. Loops in polymer networks. *Macromolecules* **52**, 4145-4153 (2019).
36. Mita, I. & Horie, K. Diffusion-Controlled Reactions in Polymer Systems. *J. Macromol. Sci. Polymer Rev.* **27**, 91-169 (1987).
37. Pouxviel, J. C., Boilot, J. P., Beloeil, J. C. & Lallemand, J. Y. NMR-study of the sol-gel polymerization. *J. Non-Cryst. Solids* **89**, 345-360 (1987).
38. Daelemans, L., Van Paeppegem, W., D'hooge, D. R. & De Clerck, K. Excellent nanofiber adhesion for hybrid polymer materials with high toughness based on matrix interdiffusion during chemical conversion. *Adv. Funct. Mater.* **29**, 1807434 (2019).
39. Tang, J., Chen, Z., Fu, A. W. & Cheung, D. W. Capabilities of outlier detection schemes in large datasets, framework and methodologies. *Knowl. Inf. Syst.* **11**, 45-84 (2007).
40. Xia, B. et al. Preparation of silica coatings with continuously adjustable refractive indices and wettability properties via sol-gel method. *RSC Adv.* **8**, 6091-6098 (2018).
41. Yang, J., Lin, G.-S., Mou, C.-Y. & Tung, K.-L. Mesoporous silica thin membrane with tunable pore size for ultrahigh permeation and precise molecular separation. *ACS Appl. Mater. Interfaces* **12**, 7459-7465 (2020).
42. Li, J. & Mooney, D. J. Designing hydrogels for controlled drug delivery. *Nat. Rev. Mater.* **1**, 16071 (2016).
43. Oehlenschlaeger, K. K. et al. Adaptable hetero Diels-Alder networks for fast self-healing under mild conditions. *Adv. Mater.* **26**, 3561-3566 (2014).
44. Zhou, J. et al. Thermally reversible Diels-Alder-based polymerization: an experimental and theoretical assessment. *Polym. Chem.* **3**, 628-639 (2012).
45. Zhou, J., Yu, G. & Huang, F. Supramolecular chemotherapy based on host-guest molecular recognition: a novel strategy in the battle against cancer with a bright future. *Chem. Soc. Rev.* **46**, 7021-7053 (2017).
46. Harada, A., Takashima, Y. & Nakahata, M. Supramolecular polymeric materials via cyclodextrin-guest interactions. *Acc. Chem. Res.* **47**, 2128-2140 (2014).
47. Chakma, P. & Konkolewicz, D. Dynamic covalent bonds in polymeric materials. *Angew. Chem. Int. Ed.* **58**, 9682-9695 (2019).

48. Zou, W., Dong, J., Luo, Y., Zhao, Q. & Xie, T. Dynamic covalent polymer networks: from old chemistry to modern day innovations. *Adv. Mater.* **29**, 1606100 (2017).
49. St John, N. A. & George, G. A. Cure kinetics and mechanisms of a tetraglycidyl-4,4'-diaminodiphenylmethane/diaminodiphenylsulphone epoxy resin using near i.r. spectroscopy. *Polymer* **33**, 2679-2688 (1992).
50. Stockmayer, W. H. Theory of molecular size distribution and gel formation in branched-chain polymers. *J. Chem. Phys.* **11**, 45-55 (1943).

Acknowledgements

L.D.K. acknowledges the research foundation - Flanders (FWO; 1S37517N). P.H.M.V.S. and L.D. acknowledge FWO through a postdoctoral fellowship. D.R.D acknowledges FWO through G.0H52.16N and Vlaio (Catalisti) through the Moonshot initiative (ReSet Project). The computational resources (Stevin Supercomputer Infrastructure) and services used in this work were provided by the VSC (Flemish Supercomputer Center), funded by Ghent University, FWO and the Flemish Government - department EWI. The work at Stanford University was supported by the US Department of Energy, Office of Basic Energy Sciences, under contract no. DE-FG02-07ER46391. C.B.-K. acknowledges an Australian Research Council (ARC) Laureate Fellowship enabling his photochemical research program as well as the Queensland University of Technology (QUT) for key support. H. F. acknowledges ARC funding through a Discovery Early Career Researcher Award (DE200101096).

Author contributions

L.D.K, P.H.M.V.S, and D.R.D. contributed to the development of matrix-based kinetic Monte Carlo (*k*MC) simulations for network synthesis. L.D.K, P.H.M.V.S., M.F.R., and D.R.D. focused on the determination of its scale dependent model parameters and contributed to the construction of the associated structure-property relationships. D.R.D. developed the overall framework of the connection of *k*MC and molecular dynamics (MD) simulations. K.I.K. and R.H.D. contributed to the part of the MD simulations and interpretation, and the construction of the structure-property relationship for the organosilica case. L.D. and K.D.C. contributed to the experimental part on the epoxy-amine curing and the construction of the related structure-property relationship. D. K., H.F. and C.B.K. contributed to the

experimental part on the Diels-Alder network chemistry and the construction of the related structure-property relationships. All authors have approved the manuscript and made revisions along its preparation.

Additional information

Supplementary Information accompanies this paper.

Competing interests

All authors declare no competing interests.

Figures

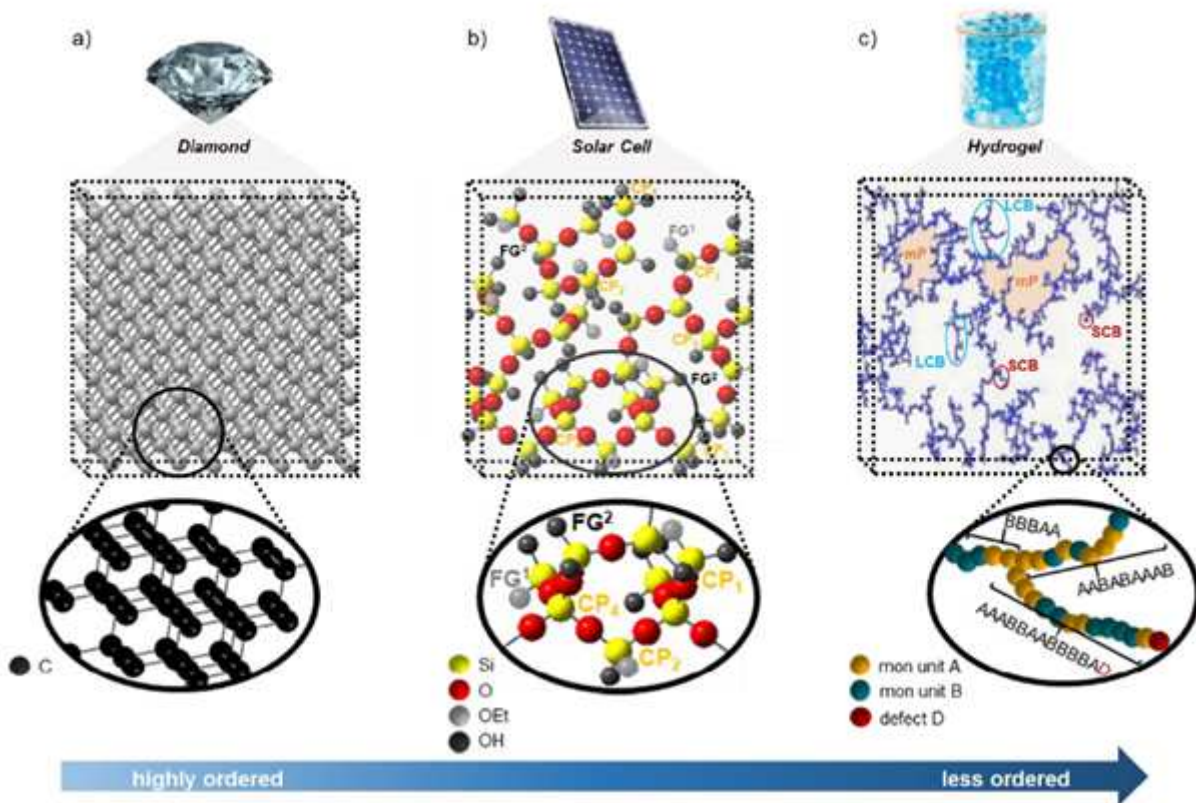


Figure 1

Network materials with decreasing order of their 3D structural configuration.

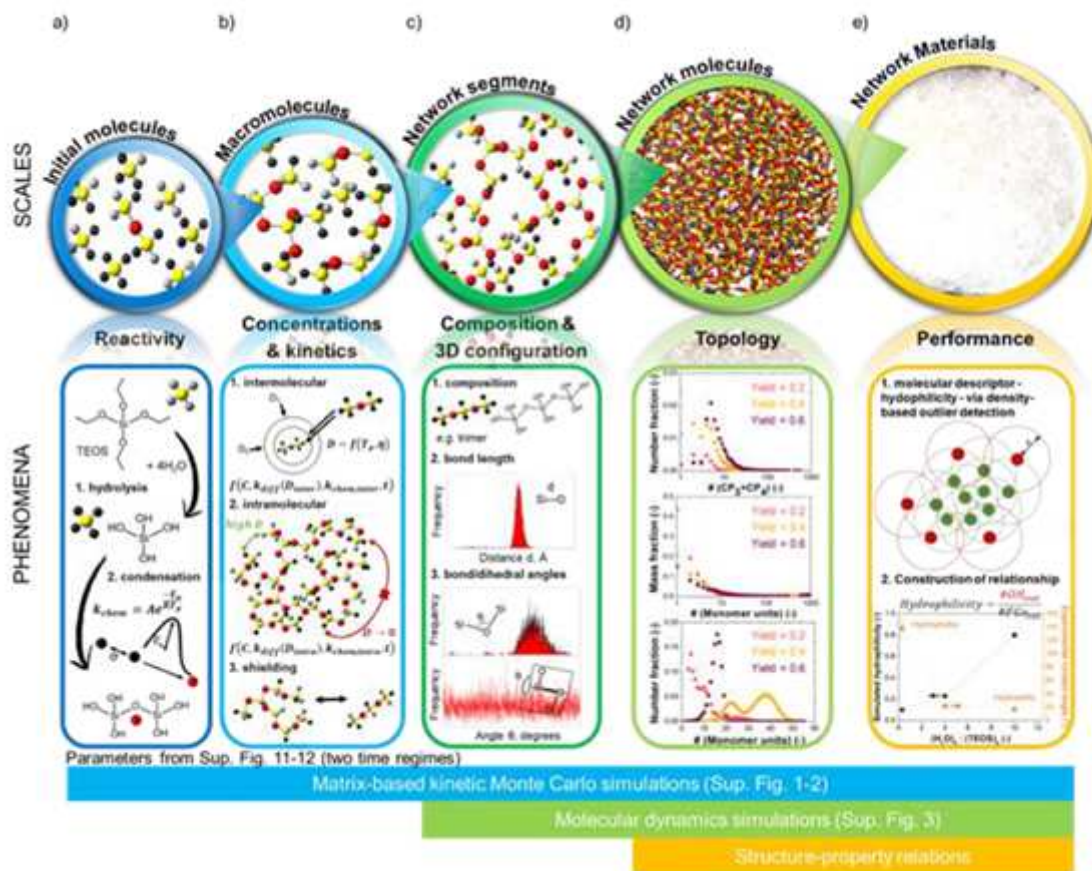


Figure 2

Main concepts of framework to design network polymer synthesis starting at the molecular scale; matrix-based kinetic Monte Carlo (kMC) and molecular dynamic (MD) simulations are interconnected to visualize the incorporation of building block by building block so each functional group (FG) at any synthesis time t ; illustration for organosilica network synthesis (Fig. 1b) commencing from tetraethylorthosilicate (TEOS).

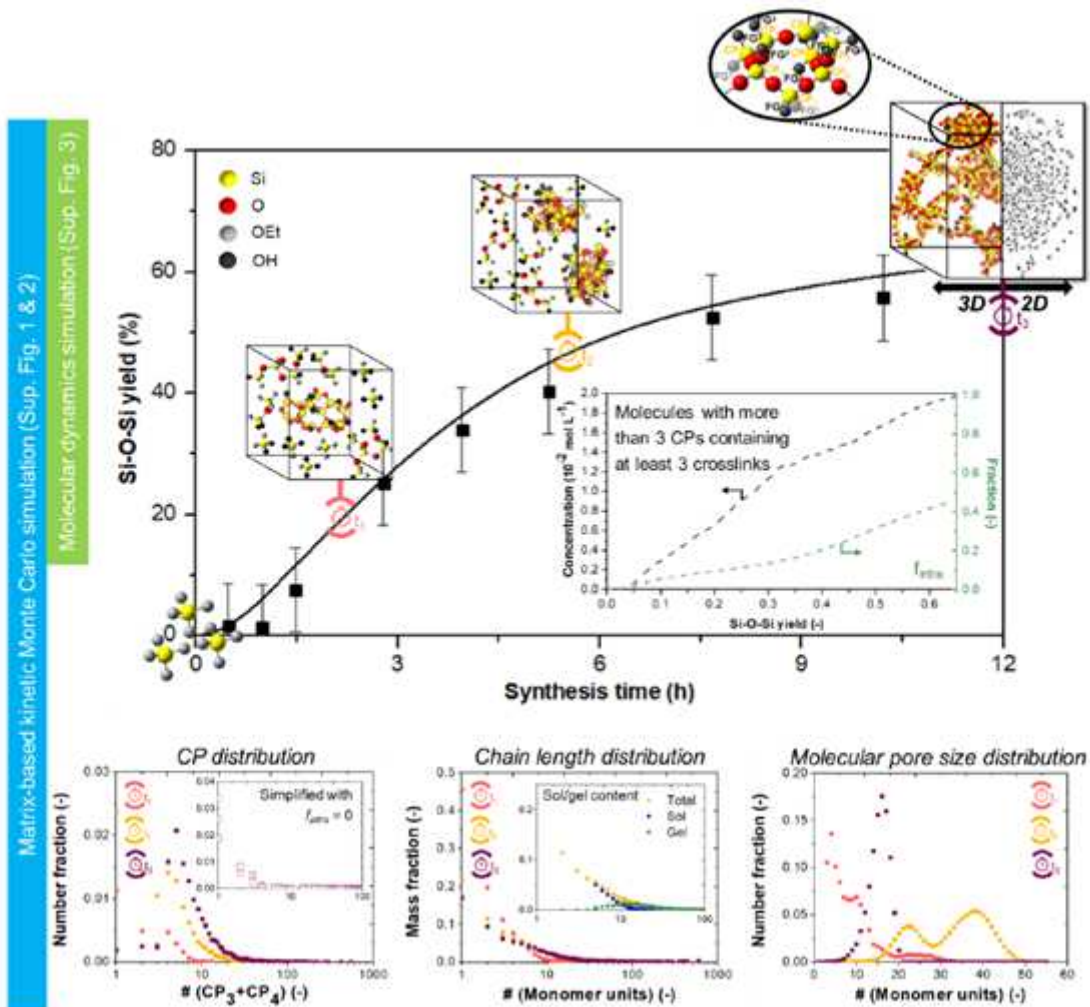
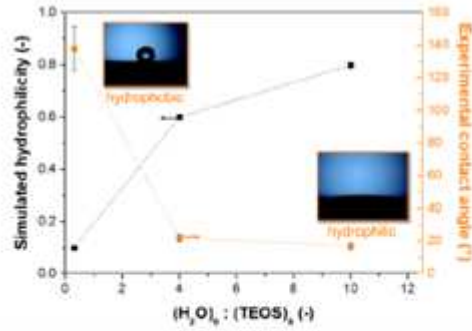
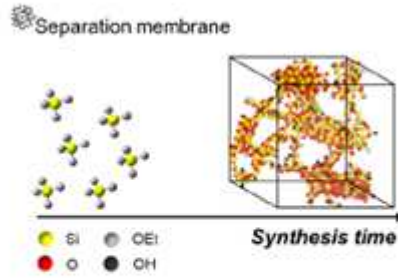


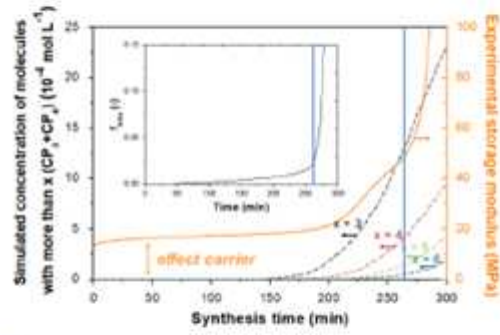
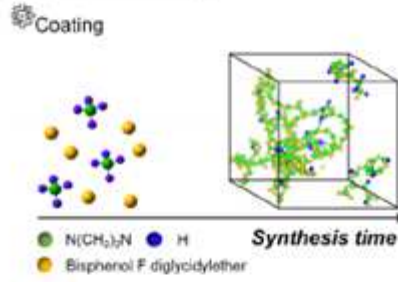
Figure 3

Strength of connecting matrix-based kinetic Monte Carlo (kMC) and molecular dynamic (MD) simulations to fundamentally understand time dependencies for organosilica network synthesis, starting from tetraethylorthosilicate (TEOS)

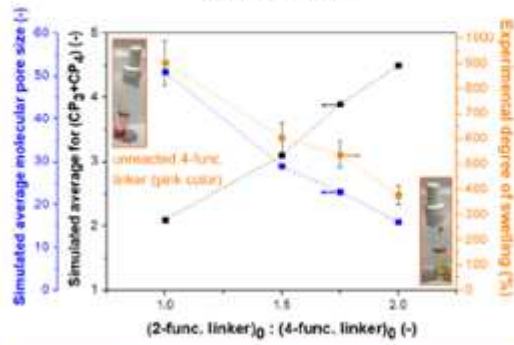
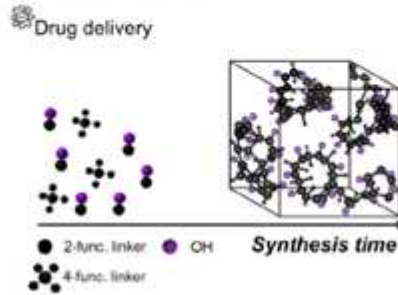
a) Organosilica synthesis



b) Epoxy/amine curing



c) Diels-Alder chemistry



Structure-property relations

Figure 4

Structure-property relationships at molecular level. a application for organosilica case (network chemistry 1; initial and model parameters: Supplementary Table 1).

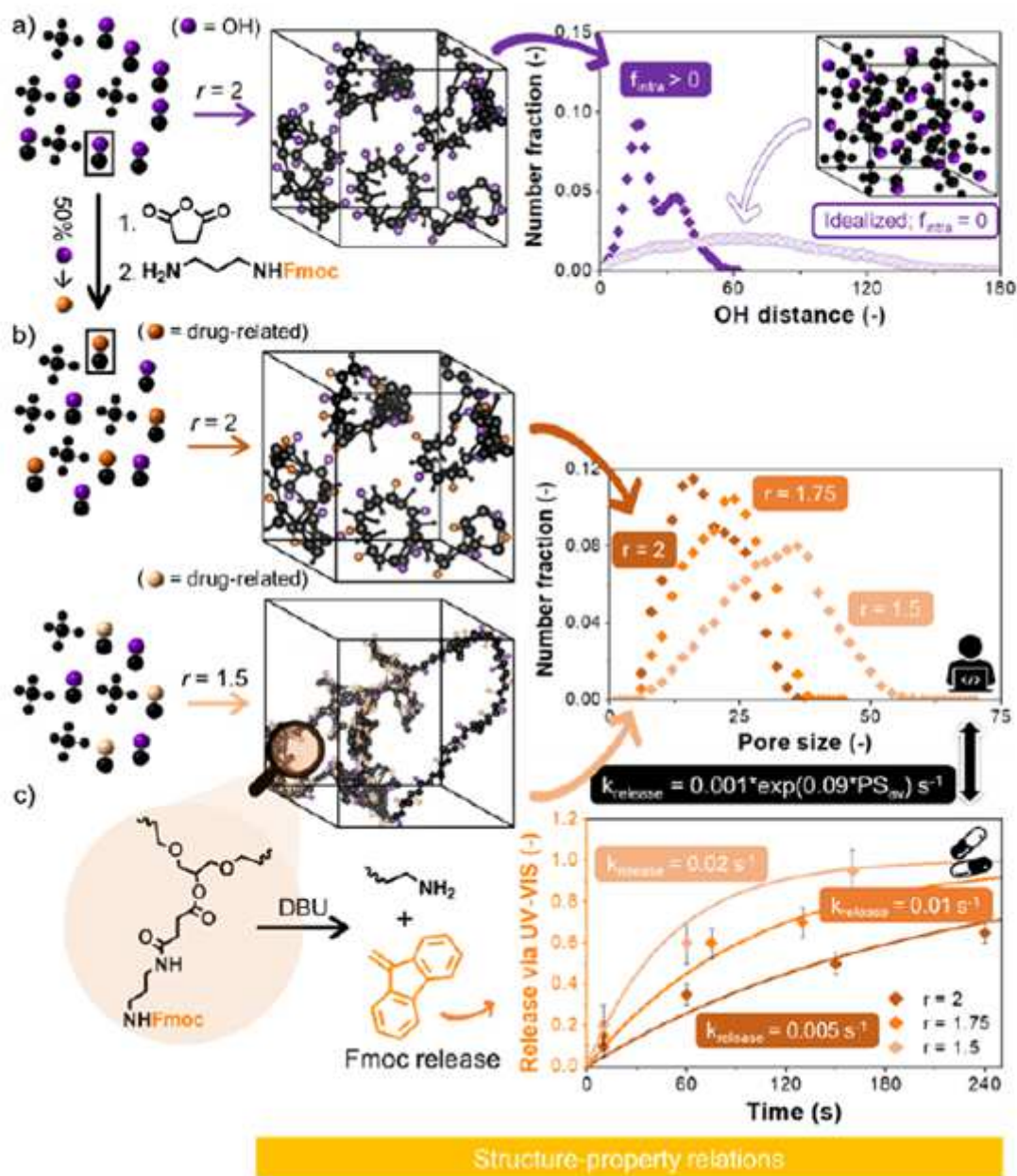


Figure 5

Relevance of non-idealities for three-dimensional (3D) Diels-Alder based network structures (chemistry 3) at final yield.

Supplementary Files

This is a list of supplementary files associated with this preprint. Click to download.

- [Sl.pdf](#)